Abrupt Permafrost Thaw Drives Spatially Heterogeneous Soil Moisture and Carbon Dioxide Fluxes in Upland Tundra

Heidi Rodenhizer, Center for Ecosystem Science and Society, Northern Arizona University, Flagstaff, AZ

Susan M. Natali, Woodwell Climate Research Center, Falmouth, MA

Marguerite Mauritz, Biological Sciences, University of Texas at El Paso, El Paso, TX

Meghan A. Taylor, Rubenstein School of the Environment and Natural Resources, University of Vermont, Burlington, VT

Gerardo Celis, Department of Anthropology, University of Arkansas, Fayetteville, AR

Stephanie Kadej, Center for Ecosystem Science and Society, Northern Arizona University, Flagstaff, AZ

Allison K. Kelley, Center for Ecosystem Science and Society, Northern Arizona University, Flagstaff, AZ

Emma R. Lathrop, Center for Ecosystem Science and Society, Northern Arizona University, Flagstaff, AZ

Justin Ledman, Bonanza Creek Long Term Ecological Research Site, University of Alaska Fairbanks, Fairbanks, AK

Elaine F. Pegoraro, Climate and Ecosystem Sciences Division Lawrence Berkeley National Laboratory, Berkeley, CA

Verity G. Salmon, Environmental Science Division and Climate Change Science Institute, Oak Ridge National Laboratory, Oak Ridge, TN

Christina Schädel, Center for Ecosystem Science and Society, Northern Arizona University, Flagstaff, AZ

Craig See, Center for Ecosystem Science and Society, Northern Arizona University, Flagstaff, AZ

Elizabeth E. Webb, School of Natural Resources and Environment, University of Florida, Gainesville, FL

Edward A.G. Schuur, Center for Ecosystem Science and Society, Northern Arizona University, Flagstaff, AZ

Keywords: Arctic, Permafrost, Abrupt Thaw, Carbon Dioxide, Soil Moisture, Fluxes

Abstract

Permafrost thaw causes the seasonally thawed active layer to deepen, causing the Arctic to shift towards carbon release as soil organic matter becomes susceptible to decomposition. Ground subsidence initiated by ice loss can cause these soils to collapse abruptly, rapidly shifting soil moisture as microtopography changes and also accelerating carbon and nutrient mobilization. The uncertainty of soil moisture trajectories during thaw makes it difficult to predict the role of abrupt thaw in suppressing or exacerbating carbon losses. In this study, we investigated the role of shifting soil moisture conditions on carbon dioxide fluxes during a 13 year permafrost warming experiment that exhibited abrupt thaw. Warming deepened the active layer differentially across treatments, leading to variable rates of subsidence and formation of thermokarst depressions. In turn, differential subsidence caused a gradient of moisture conditions, with some plots becoming consistently inundated with water within thermokarst depressions and others exhibiting generally dry, but more variable soil moisture conditions outside of thermokarst depressions. Experimentally induced permafrost thaw initially drove increasing rates of growing season GPP, R_{eco}, and NEE (higher carbon uptake), but the formation of thermokarst depressions began to reverse this trend with a high level of spatial heterogeneity. Plots that subsided at the slowest rate stayed relatively dry and supported higher CO_2 fluxes throughout the 13-year experiment, while plots that subsided very rapidly into the center of a thermokarst feature became consistently wet and experienced a rapid decline in growing season GPP, R_{eco}, and NEE (lower carbon uptake or carbon release). These findings indicate that Earth system models, which do not simulate subsidence and often predict drier active layer conditions, likely overestimate net growing season carbon uptake in abruptly thawing landscapes.

1. Introduction

Globally, permafrost-region soils contain at least 1,440-1,600 Pg carbon (Hugelius et al., 2014; Mishra et al., 2021; Schuur et al., 2018, 2022), about half of the global soil carbon stock found in other biomes (Hugelius et al., 2014; Köchy et al., 2015), and about twice as much carbon as is in the atmosphere (Houghton, 2007). Permafrost soils accumulated carbon over thousands of years due to frozen and waterlogged conditions that inhibit decomposition (Ping et al., 2015; Schuur et al., 2008). However, Arctic temperatures are rising 4 times faster than the global average (Rantanen et al., 2022), warming permafrost, causing the active layer (seasonally thawed surface soil) to deepen (Biskaborn et al., 2019; Jorgenson et al., 2006; Luo et al., 2016; Nyland et al., 2021; Romanovsky et al., 2010), and introducing previously frozen carbon to the contemporary carbon cycle (Meredith et al., 2019). In an escalating response known as the permafrost carbon feedback, newly thawed permafrost carbon is decomposed and released to the atmosphere as CO_2 and CH_4, leading to further warming (Schuur et al., 2008, 2022; Schuur & Mack, 2018).

Permafrost thaw can occur gradually as rising temperatures induce top-down thawing of permafrost or abruptly (hours to years) as geomorphological processes are triggered by melting ground ice (Kokelj & Jorgenson, 2013; Schuur & Abbott, 2011; Schuur & Mack, 2018). Abrupt thaw occurs when permafrost degrades in areas with high amounts of excess ice (ice beyond that which fits into the pore space of the soil) causing differential subsidence and the formation of thermokarst depressions (Harris et al., 1988; Lee et al., 2014). While abrupt thaw has been a cyclical part of permafrost ecosystems, the rate and extent appear to be increasing due to climate change (Farquharson et al., 2019; Jorgenson et al., 2006, 2020; Kanevskiy et al., 2017; Lantz & Kokelj, 2008; Lara et al., 2016; Swanson, 2021; Veremeeva et al., 2021; Ward Jones et al., 2019).

Abrupt thaw can cause increasingly patchy soil moisture due to the redistribution of soil water. In permafrost ecosystems, a surface water table is perched on top of permafrost, which is relatively impermeable and confines lateral flow to the active layer (Walvoord & Kurylyk, 2016). As the active layer deepens in upland permafrost sites, the water table should follow the receding permafrost, eventually resulting in drier surface soil conditions. However, when differential subsidence causes thermokarst depressions to form, the ground surface drops closer to the perched water table. Therefore, areas with limited subsidence can get drier as the water table drops, while areas with greater subsidence can get wetter as water pools (Evans et al., 2020; Jorgenson et al., 2001; Jorgenson & Osterkamp, 2005; Vogel et al., 2009). These divergent conditions can develop within meters of each other, resulting in highly variable soil moisture. With continued thaw, thermokarst depressions can eventually expand and merge, increasing hydraulic connectivity (Connon et al., 2018) and leading to uniformly drier conditions than prior to thaw. Due to spatial and temporal variability in these processes, soil moisture can vary widely as a consequence of abrupt thaw.

Although abrupt thaw is expected to occur in only about 20% of the permafrost region, these areas have exceptionally carbon-rich soils and may account for up to 50% of total circumpolar permafrost carbon (Olefeldt et al., 2016). Abrupt thaw could therefore rapidly mobilize large stocks of permafrost carbon, potentially doubling the permafrost carbon feedback (Miner et al., 2022; Turetsky et al., 2020). However, it is difficult to predict the carbon cycle response to abrupt thaw across sites due to the differential response of plant and microbial communities to shifts in environmental conditions (Abbott & Jones, 2015; Cassidy et al., 2016; Euskirchen et al., 2017; Jensen et al., 2014;

Jorgenson & Osterkamp, 2005; Kokelj & Jorgenson, 2013; Lawrence et al., 2015; Lee et al., 2011; Miner et al., 2022; Natali et al., 2021; Varner et al., 2022; Vogel et al., 2009). The overall impact of abrupt thaw on net ecosystem exchange (NEE; the net exchange of CO_2 between an ecosystem and the atmosphere) largely depends on the balance between gross primary productivity (GPP; CO_2 fixed through photosynthesis) and ecosystem respiration (R_{eco}; CO_2 respired by autotrophs and heterotrophs): NEE = GPP - R_{eco}. GPP can be suppressed or promoted by abrupt thaw via increasing nutrient availability, increasing/decreasing soil moisture, higher soil temperature and a longer unfrozen period, physical disturbance to soils, and/or delayed snowmelt (Collins et al., 2021; Euskirchen et al., 2017; Hewitt et al., 2018; Jorgenson & Osterkamp, 2005; Kelsey et al., 2021; Mauritz et al., 2017; Rodenhizer et al., 2020). At the same time, R_{eco} can also be suppressed or promoted via many of the same mechanisms, but not necessarily by the same magnitude (Abbott & Jones, 2015; Emmerton et al., 2016; Mauritz et al., 2017; Rodenhizer et al., 2022; Subin et al., 2013).

Divergent shifts in soil moisture play a particularly important role in driving carbon fluxes as permafrost thaws through the effect on oxygen conditions, nutrient and carbon availability, and soil temperatures (Kokelj & Jorgenson, 2013). Relatively drier conditions can result in higher rates of R_{eco} and GPP due to oxygen availability within the active layer, whereas waterlogged conditions can suppress R_{eco} and GPP due to anoxic conditions within the active layer (Kotani et al., 2019; Mauritz et al., 2017; Natali et al., 2015; Schädel et al., 2016). On the other hand, higher ground heat fluxes due to inundation can cause soils to warm, deepening the active layer, increasing the stock of thawed carbon and nutrients available to microbes, and even causing the formation of a talik (layers within the soil profile which remain unfrozen year-round) (Harris et al., 1988; Subin et al., 2013). These mechanisms could potentially offset lower CO_2 production as a result of low-oxygen conditions. Additionally, plant and microbial communities may respond to environmental changes at different rates or to different degrees, making changes to carbon cycling highly variable and difficult to predict (Cassidy et al., 2016; Euskirchen et al., 2017; Rodenhizer et al., 2022; Vogel et al., 2009).

In this study, we investigated the impact of soil warming, associated abrupt thaw, and increasingly patchy soil moisture conditions on growing season CO_2 fluxes at the Carbon in Permafrost Experimental Heating Research (CiPEHR) site in Healy, Alaska. The 13-year time series of this experiment provides a unique opportunity to analyze the response of CO_2 fluxes to the trajectory of initial thaw through ground subsidence and the formation of thermokarst depressions. In the initial phase of the warming manipulation, GPP increased in response to a deeper active layer and increased *Eriophorum vaginatum* biomass, which was likely responding to higher nutrient availability (Mauritz et al., 2017; Natali et al., 2011; Salmon et al., 2016). However, as continued warming and permafrost thaw caused ground subsidence and wetter soil conditions began to develop, this initial increasing trend in GPP began to level off (Mauritz et al., 2017). Similarly, R_{eco} increased with thaw depth initially, although not as strongly as GPP, and also began to level off as soil conditions became wetter (Mauritz et al., 2017; Natali et al., 2011). Building on these previous observations at this site, we explicitly focused on the response of CO_2 fluxes to the variable moisture conditions caused by abrupt thaw that continued to develop over the later phase of the experiment. With continued permafrost thaw and subsidence, we hypothesized that CO_2 fluxes in deeply subsided, wet plots would decrease, while drier neighboring plots that did not subside as deeply would maintain higher CO_2 fluxes.

2. Methods

2.1. Site and Experimental Design

The Carbon in Permafrost Experimental Heating Research (CiPEHR) is located in moist acidic tussock tundra at ~700 m in the foothills of the Alaska Range near Healy, AK. The site is underlain by permafrost due to cool temperatures at this elevation. Soils are classified as Gelisols with a ~0.45-0.65 m thick organic layer (Schuur et al., 2009). Mean annual temperature during the study was -1.71°C (2009-2021), with a growing season (May 1-Sept 30) average of 9.70°C and a non-growing season (Oct.-Apr.) average of -9.89°C (Figure S1; Table S1). Mean annual temperatures ranged from -4.08°C in 2013 (z-score = -1.50) to 1.04°C in 2019 (z-score = 1.74). Mean annual rainfall was 278 mm, with all rainfall occurring during the growing season in seven of the thirteen years. In the remaining years, 21% of annual rainfall occurred during the non-growing season in one year and less than 10% of rainfall occurred during the non-growing season in the other five. Spring snow depth ranged between 0.00 m in 2015 (z-score = -1.51) and 0.86 m in 2021 (z-score = 1.63) and the date of complete snowmelt ranged between April 17 in 2016 (z-score = -1.17) and May 27 in 2013 (z-score = 2.36).

CiPEHR was established in 2008 to simulate future warming caused by climate change by passively warming soil and air temperatures (Natali et al., 2011). Soil warming was achieved with snow fences, which increase snow depth, insulating the soil from cold winter air. Excess snow in warming treatments was shoveled off each spring to ensure similar water inputs and snowmelt dates in control and soil warming treatments (Table S1). The experiment consisted of three replicate blocks with two snow fences each. Each snow fence consisted of eight plots, four on the control side of the fence, and four on the soil warming side of the fence, for a total of 48 plots. Air warming was achieved within half of the plots on each side of the snow fences using 0.36 m^2 x 0.5 m tall clear open-top chambers (OTCs) which were deployed during the snow free period.

This experiment was designed with four discrete treatments: control, air warming, soil warming, and air + soil warming. Over the course of the experiment however, differential ground subsidence related to heterogeneous ground ice distribution and experimental warming resulted in a wide range of environmental responses (Rodenhizer et al., 2020). Environmental conditions did not respond uniformly within treatments; rather a gradient of responses developed both across and within treatments. To make full use of this gradient of environmental responses in explaining CO_2 fluxes, we used either a classification of plots based on thermokarst status or continuous environmental explanatory variables throughout most analyses rather than considering the original treatments as categorical effects.

2.2. Environmental Monitoring

Meteorological variables were monitored using a HOBO Onset station (Bourne, MA, USA) that reported half-hourly mean values. Air temperature was measured year-round at 2 m, photosynthetically active radiation (PAR) was measured year-round, and rainfall was measured during the growing season. Missing data were gap-filled using an eddy covariance tower and meteorological tower located 1 km away (Schuur et al., 2021) or nearby NOAA climate stations when necessary. Growing degree days were calculated as the cumulative sum of temperatures above 0°C, and freezing degree days were calculated as the cumulative sum of temperatures below 0°C on an annual basis. Cumulative end-of-season snow depth was measured along transects located at each fence (control and soil warming) in April immediately prior to snow shoveling. Chamber air temperatures were measured during CO_2 flux measurements at 15 cm height within each OTC using shaded thermistors and were gap-filled using plot-level linear models with the HOBO air temperature (r2: min = 0.90, mean = 0.92, max = 0.93).

Permafrost thaw was monitored with measurements of soil temperature, thaw depth, and subsidence. Soil temperature was measured at 5 and 10 cm depths in all plots and at 20 and 40 cm depths in half of the plots of each treatment using type T copper-constantan thermocouples. Thaw depth was measured once or twice weekly throughout the snow-free season using a metal probe and active layer thickness (ALT) was calculated as the deepest annual thaw depth measurement. Elevation was measured at point locations in a 2x2 m grid across each of the experimental blocks using a Trimble (Westminster, CO, USA) high-precision differential GPS in late July or early August of 2009, 2011, and 2015-2020 (Rodenhizer et al., 2020). A continuous elevation surface was created for each year using ordinary kriging and subsidence was calculated as the difference in elevation relative to 2009 (Hiemstra et al., 2009). Plot-level subsidence was gap-filled in years without measurements using linear interpolation. Thaw penetration was calculated as the sum of subsidence and ALT.

Soil moisture conditions were monitored with measurements of soil moisture at two depths and water table depth. Surface moisture was estimated in the top 5 cm of the moss/soil layer in each plot using site-calibrated DC half-bridge resistance measurements (Vogel et al., 2009). The sensors used for surface moisture did not produce exact values, but the relative values between measurements can be compared. Soil moisture was measured in the top 15 cm in half of the plots of each treatment using Campbell Scientific CS616 water content reflectometer probes calibrated to the site. Water table depth relative to the moss/soil surface was measured manually three times weekly throughout the snow-free season (May 1- Sept 30 except when frozen) in wells that were installed at each fence throughout the experiment (minimum 4 wells per snow fence initially). Because water table depth was measured in wells which were not located within plots, water table depth values were assigned to plots by a combination of proximity and representative microtopography.

Aboveground plant biomass (AG Biomass) was estimated at the plot level using a non-destructive point-intercept method during July in 2009-2013, 2017, and 2021 (Salmon et al., 2016; Schuur et al., 2007). Point-intercept counts were completed for each species of vascular plant and for all mosses combined. Vascular biomass was dominated by the tussock forming sedge *Eriophorum vaginatum*, and other common plant species included *Vaccinium uliginosum*, *Betula nana*, *Carex* *bigelowii*, *Rubus chamaemorus*, *Empetrum nigrum*, *Rhododendron subarcticum*, *Vaccinium vitis-idaea*, *Andromeda polifolia*, and *Oxycoccus microcarpus*. We did not distinguish between moss species for this study, but the dominant species at the site included *Sphagnum fuscum*, *Pleurozium schreberi*, and *Dicranum* spp. (Deane-Coe et al., 2015).

2.3. Carbon Flux Measurements and Processing

Automated systems were used to measure growing season NEE in each experimental block (Mauritz et al., 2017; Natali et al., 2011). Each system consisted of eight flux chambers, which were rotated between 22 plots with permanently installed collars (16 within CiPEHR and 6 within a co-located experiment not considered in this study) every couple of days, such that each plot had a measurement chamber approximately one third of the time. To measure fluxes, air was circulated between the chamber and an infrared gas analyzer (LI-820, LICOR corp., Lincoln, NE, USA) for 1.5 minutes and CO_2 concentration was measured every 2 seconds. Flux rates were calculated using linear regression and converted from volumetric units (ppm CO_2 m^{-2} s^{-1}) to mass units (µmol CO_2 m^{-2} s^{-1}) using chamber specific volume and temperature. Measurements were logged on a Campbell Scientific CR1000 data logger. The system cycled continuously through all chambers, such that each chamber was measured every 1.6 hours. In 2019, a smaller subset of plots (n = 12) were measured in order to reduce field work effort. To maximize the range of environmental conditions and fluxes represented by the subset of plots that were measured in 2019, we selected plots across the entire range of mean annual water table depth and ALT (water table depth range: -30 cm to 13 cm; ALT range: 67 cm - 133 cm). This resulted in a bias in the treatment-level flux estimates in 2019 as compared to years when we measured all plots. We reduced this bias by gap-filling missing plot-level fluxes to determine annual averages for 2019 using relationships with environmental conditions (see 3.6.2).

All processing of carbon flux data was performed in R (R Core Team, 2021) using the data.table (Dowle & Srinivasan, 2021) and tidyverse packages (Wickham et al., 2019). Flux modeling for gap-filling and flux partitioning was completed using the minpack.lm package (Elzhov et al., 2016). CO_2 flux was calculated as the slope of CO_2 concentration throughout the measurement period (ppm CO_2 s^{-1}) and converted to NEE (µmol m^{-2} s^{-2}) using the chamber volume and air pressure. Raw flux measurements were filtered to remove erroneous measurements. All measurements with unrealistic CO_2 concentrations (<300 ppm or >550 ppm), low chamber air flow rate (<500 mL min^{-1}), or during periods of high wind speeds (>7 m s^{-1}) were removed. Additionally, all flow rates, CO_2 concentrations, and CO_2 fluxes were visually inspected in ~10 day periods to remove outliers.

In order to estimate continuous half-hourly flux in each plot, we gap-filled NEE using a light response curve with PAR,

$$\text{Eq. 1. } NEE = \frac{a \times PAR \times GPmax}{(a \times PAR) + GPmax} + R$$

where a is photosynthetic efficiency, or the photosynthetic rate at half of GPmax, GPmax is the maximum potential photosynthetic rate, and R is the basal rate of respiration. In order to allow for differences between plots (caused by treatment or natural variability) and throughout the growing season, NEE was modeled monthly in each plot throughout the growing season (May-Sept.). Only measurements taken during the day were included in this modeling step. For the purposes of modeling, day was defined as PAR ≥ 5 µmol m^{-2} s^{-2} and night as PAR < 5 µmol m^{-2} s^{-2}. With this threshold, 0.06% of nighttime NEE measurements showed carbon uptake. The resulting parameters were used to gap-fill missing measurements.

R_{eco} was modeled at the plot-level using a temperature sensitivity (Q10) model with soil temperature at 10 cm depth,

$$\text{Eq. 2. } R_{eco} = A^{B \times T_{soil}}$$

where A is the basal respiration rate and B is the Q10 temperature response. NEE measurements taken at night were assumed to be R_{eco} without any contribution from photosynthesis and were used for this modeling step. The resulting parameters were used to both gap-fill missing nighttime respiration measurements and estimate daytime respiration.

GPP was estimated as

$$\text{Eq. 3. } GPP = NEE - R_{eco}$$

during the day (PAR≥5) and was set to 0 during the nighttime. This method resulted in some negative values for GPP. Though not biologically meaningful, these negative values reflect uncertainty associated with the measurements and models and were left in the dataset in order to avoid overestimating flux sums.

We estimated plot-level non-growing season (Oct.-Apr.) respiration using a soil temperature response curve determined at an eddy covariance tower at the site (Schuur et al., 2021). Half-hourly winter respiration measured at the eddy covariance tower was modeled using the ecosystem respiration Q10 model (Eq. 2.) with 5 cm soil temperature. These parameters were used to estimate half-hourly fluxes for each plot using plot-level 5 cm soil temperature measurements. Although we did not account for shoulder season photosynthesis in our modeling approach, this is unlikely to change the sign of the annual carbon balance, as April and October GPP combined tended to be less than 15 g C m^{-2} at the site (Schuur et al., 2021; Webb et al., 2016), an order of magnitude less than modeled annual CO_2 emissions.

2.4. Data Merging and Derived Variables

All environmental and flux data were aggregated to monthly and annual values. We defined a year as Oct. 1st to Sept. 30th so that the environmental conditions of the prior winter could be considered when modeling fluxes. Fluxes and precipitation were summed, and for all other environmental data, the mean and standard deviation were calculated. The standard deviation was included as a metric of intraseasonal variability within individual plots. Additionally, we calculated time-lagged mean surface moisture, mean soil moisture, and growing degree days for the current and prior months to infer the effect of antecedent conditions on fluxes.

2.5. Thermokarst Classification

Plots were classified according to their thermokarst status in 2017-2019 and 2021 following the methods in Rodenhizer et al. (2022), in order to condense environmental conditions such as the degree of thaw and moisture conditions into a categorical variable that reflected real-world environmental conditions better than the original treatments, reducing within-class variability. The classification used 1 m airborne LiDAR data from the National Ecological Observatory Network (NEON) to classify each plot as non-thermokarst (Non-TK), thermokarst-margin (TK-margin), or thermokarst-center (TK-center), where TK-centers were cells where the elevation fell below the local median elevation and TK-margins were any cells within 1 m of a thermokarst depression outline (NEON (National Ecological Observatory Network), 2022). To determine thermokarst classifications in 2020, when LiDAR data were not available, we gap-filled on a plot by plot basis using linear interpolation of the classes coded as integer values.

2.6. Flux Analysis

We used gradient boosted regression tree models (hereafter regression trees) to investigate environmental drivers of CO_2 fluxes directly, as these environmental drivers were the result of unpredictable abrupt thaw processes on top of the plot treatments. This approach allowed a mechanistic understanding of the role of permafrost thaw in driving CO_2 fluxes as well as solving the issue of increasing variance through time seen in the various categorical approaches to analyzing this dataset. This machine learning method was chosen because it allows for non-linear relationships and was completed using the gbm package in R (Greenwell et al., 2020). Data from 2009 were not included in the flux analysis, because CO_2 fluxes were lower than expected, likely due to disturbance from experimental set-up activities (Celis et al., 2017; Mauritz et al., 2017). We modeled GPP, NEE, and R_{eco} separately using cumulative monthly (*n* = 6912) and cumulative growing season (*n* = 576) fluxes from each plot. The variables included in the monthly models were the mean and standard deviation of surface moisture, soil moisture, water table depth, and soil temperature (10 cm), as well as thaw depth, annual subsidence, thaw penetration to date (thaw depth + annual subsidence), monthly precipitation sum, monthly growing degree days, monthly freezing degree days, annual AG Biomass, mean air temperature, 2 month surface moisture, 2 month soil moisture, and 2 month growing degree days. The explanatory variables included in the cumulative growing season models were thaw penetration, subsidence, ALT, total precipitation, previous winter snow depth, previous winter minimum soil temperature (10 cm), AG Biomass, and the mean and standard deviation of surface moisture, soil moisture, water table depth, air temperature and soil temperature (10 cm). The standard deviation of certain environmental variables were included as explanatory variables to account for temporal variability, as we hypothesized that landscape position would impact the consistency of environmental conditions. For example, soil moisture, water table depth, and soil temperature might be more consistent in TK-centers, where water pools, than in other landscape positions that could experience drastically different conditions immediately following rain or after a few days of dry, sunny weather.

We determined the optimal number of trees, interaction depth, shrinkage, and minimum observations per node from a range of values using the caret package (Kuhn, 2021). 80% of the data were randomly sampled for model training and the remaining data were reserved to evaluate model performance. Model performance was evaluated using a linear regression of the predicted vs. measured values; slope of lines were determined by geometric mean regression, which splits the variance equally between both axes. Relative influence (RI; reduction in the sum of squared error attributable to each variable and normalized to sum to 100) was used to evaluate the importance of model predictors. Partial dependence plots were used to evaluate the effect of the top predictors on CO_2 fluxes, and Shapley additive explanations were used to investigate differences in model behavior in the driest and wettest deeply thawed plots.

To evaluate the trajectory of CO_2 fluxes according to the degree of abrupt thaw, we visualized growing season CO_2 flux time series in each thermokarst class. The plots were binned according to their thermokarst class in the final year, allowing the plots to be grouped by the rate at which they are thawing. Additionally, we gap-filled monthly NEE, R_{eco}, and GPP in 36 plots which were not measured in 2019 using the monthly regression trees and observed environmental conditions. We plotted splines (Generalized Additive Models) to observe trends through time.

3. Results

3.1. Flux Response to 13 Years of Warming

Growing season CO_2 fluxes responded non-linearly to warming over time. Early on, warming plots showed higher net carbon uptake than control plots, but this pattern weakened or reversed later in the experiment, particularly in the soil warming treatment (Figure 1). Soil warming plots had the largest increase in NEE, GPP, and R_{eco} initially while air warming had the smallest increase, with an intermediate response in air + soil warming plots. The treatment effect peaked in the 5th year for all treatments and fluxes and declined thereafter. Between years 6 and 13, GPP remained somewhat elevated in the air + soil warming treatment, R_{eco} was reduced in the air warming treatment, and NEE was consistently reduced in soil warming plots (lower growing season carbon uptake) relative to control. All treatments experienced increasing variability through time, indicating that feedbacks associated with warming had divergent impacts on individual plots. No statistics are included here due to this heteroscedasticity.

3.2. Environmental Changes Associated with Experimental Warming

ALT increased over time, particularly in the soil warming plots, and this caused ground surface subsidence and increasingly wet soil conditions (Figure 2; Figure S2; Table S2). However, there was considerable variability among plots in the trajectory of thaw, subsidence and water table based on pre-existing differences in ground ice content. At the beginning of the experiment, ALT was very consistent between plots, with a mean of 55 ± 4 cm (mean ± standard deviation). By year 13, mean ALT was 140 ± 40 cm (change: 85 ± 40 cm, p-value = 2.2×10^{-16}), with considerable overlap between control and soil warming plots and much higher variability than initially. Air warming did not have a significant effect on ALT by year 13. On average, the site became wetter, as water table depth shifted from 26.5 ± 6.0 cm below the soil surface to 12.5 ± 10.0 cm below the soil surface by the end of the experiment (change: 14.0 ± 11.5 cm, p-value = 6.6×10^{-13}), but this average response was again composed of divergent responses across plots. All but two plots became wetter, with a few of the plots becoming fully inundated with standing water. The remaining dry locations tended to experience high temporal variability in water table depth, while wet locations had consistently shallow water table depth (Figure S2, Figure S3).

Rising regional air temperatures caused thermokarst in the control plots and outside of the experimental footprint (Schuur et al., 2021), and experimental warming accelerated the formation of thermokarst in the soil and soil + air warming plots (Figure 3). Photos taken during experimental set-up indicate that there were no thermokarst depressions within the experimental footprint (Figure

S4). By year 9, about half of the plots (all of the soil and soil + air warming, plus one control plot) were located along a TK-margin or within aTK-center. By year 13, over 75% of the plots were located along a TK-margin or within a TK-center, including over half of control and air warming plots.

Moving beyond treatment effects to analyze the environmental conditions of thermokarst classes, we saw that plots showed increasing thaw and wetter conditions in and near thermokarst depressions within the experimental footprint, although differences were not always statistically significant due to increasing variability (Figure 4A, B, D, E, and H). The increasing between-plot variance in environmental conditions indicated that these classes, although better than treatment bins, were still insufficient to describe the wide variety of observed environmental changes. ALT was shallowest in initial conditions (60.5 ± 3.0 cm; mean ± standard deviation). During years 9 -13, ALT deepened by 17 cm in Non-TK (78.0 ± 13.5 cm), nearly doubled in TK-margins (110.0 ± 31.0 cm), and more than doubled in TK-centers (132.0 ± 33.0 cm). Similarly, subsidence increased from Non-TK (10 ± 9 cm), to TK-margins (33 ± 20 cm), and TK-centers (52 ± 18.5 cm), with increasing between-plot variance through the classes. Metrics of soil moisture (surface moisture, soil moisture, water table depth) showed that TK-centers were wetter than other classes, whereas differences between other classes were not statistically different. Water table depth was 20 ± 4 cm below the surface initially. Within TK-centers, mean water table depth was 4 ± 8 cm below the surface and some plots were flooded.

Intraseasonal variability in metrics of soil moisture showed inconsistent patterns across classes (Figure 4C, F, and I). All classes had similar intraseasonal variability in surface moisture and soil moisture except TK-centers, where it was higher and more variable across plots. Intraseasonal variability in water table depth was lowest in TK-centers and highest in Non-TK, with the other classes falling in between (Initial: 5 ± 1 cm; Non-TK: 7 ± 2; TK-margins: 6 ± 3 cm; TK-centers: 6 ± 2 cm).

We also observed increasing variability in AG Biomass as subsidence progressed, although there were no statistically significant differences in the mean values between groups (Figure 4G). AG Biomass was slightly lower in initial conditions (451 ± 86 g m^{-2}) compared to Non-TK (514 ± 130 g m^{-2}), TK-margins (531 ± 134 g m^{-2}), and TK-centers (531 ± 197 g m^{-2}). The spread in AG Biomass between plots increased dramatically in TK-centers, with some plots losing all biomass, and others showing some of the highest AG Biomass of the experiment. The loss of biomass in some plots was related to increasing soil moisture and inundation (Figure S5).

3.3. CO_2 Fluxes

3.3.1. CO_2 Flux Response to Thermokarst

Investigating growing season cumulative CO_2 fluxes in relation to thermokarst classes revealed a non-linear response to soil warming and permafrost thaw over time. Across all thermokarst classes, cumulative growing season CO_2 fluxes increased in the first four years of the experiment, but showed divergent responses thereafter (Figure 5). In Non-TK, both GPP and R_{eco} continued to increase throughout the experiment, although the rate of increase declined slightly near the end, particularly for GPP (Table S3). Growing season NEE in Non-TK plots increased through year 10, plateauing around growing season net CO_2 uptake of 86 gC m^{-2}. In TK-margins, both GPP and R_{eco} increased at the beginning of the experiment followed by decline, although the rate of both the increase and decrease were lower for Reco than for GPP. Overall, growing season NEE in TK-margins increased more strongly than Non-TK through year 7, reaching a peak of 117 gC m^{-2}, but then declined to 90 gC m^{-2} by year 13, slightly higher than the beginning of the experiment. In TK-centers as well, GPP increased more rapidly than Reco initially and then declined more rapidly than Reco. Overall, growing season NEE in TK-centers increased through year 5, peaking at 124 gC m^{-2}, then decreased through year 13, falling to about 55 gC m^{-2}, similar to initial values. Additionally, a few plots located in TK-centers showed consistent, strong net carbon release (negative NEE) throughout the growing season in the last several years of the experiment.

3.3.2. Environmental Drivers of CO_2 Fluxes

Both treatments and thermokarst classes showed highly variable plot-level trajectories in environmental variables, likely due to stochastic factors such as differences in ground ice distribution at the beginning of the experiment and proximity to thermokarst initiation sites. By analyzing all plots individually using continuous environmental variables, the effect of these drivers on carbon fluxes could be considered explicitly. The regression tree models showed good fit, and highlighted the importance of biomass, moisture and temperature variables in driving growing season CO_2 fluxes (Figure 6). At the monthly timescale where seasonality plays a strong role, the validation regression r^2 values were 0.83, 0.73, and 0.81 for GPP, NEE, and R_{eco}, respectively, while at the cumulative growing season timescale, the values were 0.50, 0.43, and 0.52, respectively. All of the models had a tendency to slightly overestimate low fluxes and underestimate high fluxes (deviation from the 1:1 line); this bias was larger in the cumulative growing season models.

At the monthly timescale, the top predictor of all CO_2 fluxes was either air or soil temperature (Figure 6; GPP, NEE: air temperature; R_{eco}: soil temperature). With relative importance (RI) values above 30, temperature had much greater influence than the next predictor in all models, AG Biomass, which had RI values around 10. Higher temperatures and AG Biomass drove higher fluxes in all cases (Figure S6). Two variables related to water availability showed up in the top 4 predictors of monthly CO_2 fluxes; NEE dropped as soil moisture increased above 70% (RI = 5) and R_{eco} dropped as subsidence increased (RI = 6). Additionally, the 5th predictors of GPP and R_{eco} were related to water availability (GPP: standard deviation of surface moisture, RI = 4; R_{eco}: water table depth, RI = 5).

At the cumulative growing season timescale, where annual and plot differences, rather than seasonality, prevail, the top predictor of all CO_2 fluxes was biomass, with RI values between 15 and 30 (Figure 6). For NEE, the remaining top predictors were related to water availability and variation, with RI values between 6 and 9 (soil moisture, standard deviation of surface moisture standard deviation of soil moisture). GPP and R_{eco} responded similarly, and non-linearly, to metrics of permafrost thaw and water availability, with RI values between 6 and 13 (GPP: ALT, water table depth, spring snow depth; R_{eco}: ALT, water table depth, subsidence; Figure S7). For mean soil moisture and water table depth, the responses were characterized by linear increases at moderate values and a rapid decline in extremely wet conditions. The response to moisture variability differed by depth; NEE was lowest at moderate values of variability in surface moisture and higher at both extremes, while the opposite was true for variability in soil moisture. Finally, both GPP and R_{eco} increased with ALT up to about 125 cm, beyond which the relationship plateaued.

4. Discussion

Experimentally-induced permafrost thaw resulted in a patchwork of thermokarst depressions and variable soil moisture (Figure 7: ‘early thaw’) as a result of experimental warming effects combined with pre-existing plot-level differences in attributes such as ground ice content. This created a continuum from relatively shallow thaw and drier, but highly variable, soil moisture conditions to deeper thaw and wet conditions. The deepest thaw depths increased ALT by >300% over the course of the experiment, primarily in response to soil warming and climate change; the air warming treatment did not have a detectable impact. Even in the face of rising mean water table depths, the response of water table depth ranged from dropping below initial values (20 cm depth) in two plots all the way to rising above the soil surface in others. The environmental trajectories of individual plots had a cascading effect on CO_2 fluxes: initial increases in growing season NEE, GPP, and R_{eco} were smallest outside of thermokarst features (less thaw) and largest in plots that developed into TK-centers (more thaw), but wet conditions which developed in TK-centers drove a rapid reversal in this trend later in the experiment. In the drier conditions that were common early in the experiment and remained in some plots throughout the entire experiment, experimental warming promoted GPP more than R_{eco}, leading to higher net growing season carbon uptake. As thermokarst depressions formed mid- to late in the experiment, wet conditions suppressed GPP more than R_{eco}, causing the wettest plots to release carbon over the growing season. These findings add experimental evidence to the growing body of literature that changes in surface hydrology linked to abrupt permafrost thaw, which has generally not been included in Earth System Models used in IPCC projections, is likely to amplify permafrost carbon release in response to warming, and may reduce the ability of plants to offset these emissions (Ekici et al., 2019; IPCC, 2021; Lee et al., 2014; Schädel et al., 2018; Schuur et al., 2021).

4.1. Non-Linear Carbon Flux Responses To Divergent Hydrologic Conditions

Early in the experiment, warming and permafrost thaw increased all growing season C fluxes, but as individual plots subsided at different rates, likely due to differences in ground ice distribution, divergent soil moisture conditions altered the response of CO_2 fluxes (Mauritz et al., 2017; Natali et al., 2011). The initial increase in NEE in thawing plots was likely caused by the mobilization of carbon and nutrients in the deepening active layer that stimulated GPP more than R_{eco}. In the first 5 years of the experiment, foliar N pools increased by 49% and AG biomass increased by 23% in soil warming plots, with over 90% of the increase in biomass occurring in Eriophorum vaginatum (Salmon et al., 2016).

By the middle of the experiment, declines in NEE were linked to greater subsidence and increasingly wet conditions which reduced GPP more than R_{eco}. By the end of the experiment, GPP and R_{eco} were suppressed in consistently wet plots, leading to lower growing season carbon uptake, or even net carbon release, the opposite response to thermokarst as was previously found at the landscape level surrounding this site (Rodenhizer et al., 2022). In contrast, both GPP and R_{eco} were higher along moderately-subsided TK-margins where thaw was deep but soils were not waterlogged, leading to higher net growing season carbon uptake, the same response as previously reported (Rodenhizer et al., 2022). This indicates that TK-margins may dominate the CO_2 flux response at the landscape scale and/or the differentTK-center response may be explained by differences in thermokarst age and morphology. In the landscape surrounding the experiment, linear water tracks are common thermokarst features where water perched on the thaw table drains off the shallow hillslope. Some of these water tracks are decades old and exhibit higher plant biomass, GPP, and R_{eco}, as plant community succession has promoted sedge and moss growth of species tolerant of the waterlogged conditions, with larger shrubs confined to deeply thawed and relatively dry TK-margins (Osterkamp et al., 2009; Rodenhizer et al., 2022; Schuur et al., 2009). Within the decade-long warming manipulation, however, subsidence has formed discrete features related to the experimental plots, and these features have neither coalesced as water tracks, allowing drainage, nor undergone plant community succession as of yet. Rather, plants have died in the most deeply-subsided, waterlogged TK-centers, a few which are inundated much of the year (Figure 4; Figure S5), with Eriophorum vaginatum surviving the longest in inundated conditions. This decrease in plant biomass, combined with waterlogged soil conditions, explains lower GPP and R_{eco} observed in TK-centers in this study (Mauritz et al., 2017; Schädel et al., 2016). This is in contrast to other drier sites, where increased soil moisture can alleviate drought conditions (Emmerton et al., 2016; Euskirchen et al., 2017).

Increased plant biomass in water tracks combined with drier conditions along water track margins may dominate the growing season flux response to abrupt thaw at the landscape scale as observed by the eddy tower (Rodenhizer et al., 2022). However, this may not be sufficient to offset increases in R_{eco} during the winter (Table S4). Our estimates suggest the potential for permafrost thaw to shift these ecosystems towards becoming carbon sources at the annual scale, as found in a number of previous studies using a variety of methods (Cassidy et al., 2016; Hicks Pries et al., 2013; Rodenhizer et al., 2022; Schuur et al., 2021; Turetsky et al., 2020). Using information from the experimental plots, modeled R_{eco} for the non-growing season more than offset growing season CO_2 uptake in most plots, resulting in calculated net release of 113 gC m^{-2} yr^{-1} on average across all plots and years (Figure S8; Table S4). Additionally, when modeled non-growing season R_{eco} was included, total annual R_{eco} was still increasing by year 13 in Non-TK plots, and showed slower post-peak declines in plots classified as TK-margins or TK-centers. This suggests that the effect of warming and permafrost thaw on non-growing season R_{eco} could be longer lasting than impacts on growing season fluxes alone. It is important to consider that non-growing season fluxes were modeled using only temperature by necessity in this calculation. A comprehensive analysis of non-growing season fluxes would need to take soil moisture into account, but this back-of-the-envelope calculation is still valuable for assessing the impact of abrupt thaw on annual ecosystem C balance. Our modeled non-growing season results are similar to several other studies from this site that used a variety of methods and found that winter respiration is responsible for shifting the ecosystem from a growing season CO_2 sink to an annual CO_2 source (Celis et al., 2017; Natali et al., 2011; Schuur et al., 2021; Webb et al., 2016). Taken together, this highlights the importance of winter respiration in determining the sign of annual carbon fluxes across the circumpolar region and the role that abrupt thaw is likely to play in amplifying non-growing season respiration (Natali et al., 2019).

4.2. Environmental Drivers of CO_2 Fluxes

Environmental drivers of CO_2 fluxes differed between the monthly and cumulative growing season models. In the monthly models, biomass and variables that reflect seasonal variability made up the majority of top predictors. The relationships between these variables and CO_2 fluxes have been long-recognized and extensively studied (Baldocchi et al., 2001; Huxman et al., 2003; Niu et al., 2011), so we chose instead to focus our discussion on the role of permafrost thaw- and soil moisture-related variables.

4.2.1. Trade-Off Effects of ALT and Inundation on Carbon Fluxes

As the landscape became increasingly patchy due to differential subsidence, individual plot trajectories diverged, even within the same treatment. Increasing variability within treatments indicated that these labels were insufficient to explain the complexity of the responses to warming. Although TK classes could capture the variability in responses better than the original treatment labels, we still observed increasing variability within classes over time. Therefore, our environmental driver analysis relied on continuous variables to utilize this variability. ALT and metrics of soil moisture were identified as two important abiotic drivers of CO_2 fluxes, and these two positively-correlated drivers had opposing effects on CO_2 fluxes, particularly R_{eco}.

In general, increasing ALT resulted in higher soil moisture (Figure 2) through ground subsidence and the redistribution of water perched on the permafrost surface (Figure 4). ALT increases were associated with higher GPP and R_{eco}, likely reflecting increased nutrient and carbon availability as permafrost thawed, in addition to higher soil temperature and a longer thawed period (Mauritz et al., 2017). Subsidence (which results in wetter soils), water table depth above the soil surface, and high values of soil moisture, on the other hand, were associated with lower NEE, GPP, and R_{eco}, likely reflecting increasingly anoxic conditions (Mauritz et al., 2017; Taylor et al., 2021). The opposite, and relatively strong, effects of these environmental variables on R_{eco} indicated that there was a trade-off between permafrost thaw mobilizing carbon and nutrients for decomposition and plant growth on the one hand and inundated conditions limiting plant growth and aerobic decomposition on the other. In the inundated plots, R_{eco} decreased more as a result of subsidence and inundation than it increased as a result of deeper ALT, leading to suppressed respiration (Figure S9). However, GPP was reduced nearly to zero in these plots, resulting in higher net CO_2 release overall, despite suppressed respiration. In plots with very deep ALT and water table depth below the surface, the impact of increased ALT was stronger than the impact of subsidence, leading to high rates of respiration (Figure S9). However, GPP was also high in these plots, leading to higher CO_2 uptake during the growing season. Overall, the two end points of the thaw-moisture continuum we observed were 1) complete inundation which led to suppressed GPP despite deep ALT, and 2) deep thaw with dry conditions which led to higher GPP. R_{eco} and NEE were similarly suppressed in these extreme cases but to a lesser degree, indicating that GPP may be more strongly impacted by changes in moisture availability than R_{eco}, at least for the time frame of this experiment.

4.2.2. Role of Soil Moisture in Driving CO_2 Fluxes

Metrics of soil moisture were important predictors of CO_2 fluxes at the seasonal timescale, and exhibited non-linear influences on fluxes. The trend of increasing C fluxes as soil moisture increased from low to moderate values indicates alleviation of water limitation (Euskirchen et al., 2017; Zona et al., 2023), even though this site is classified as moist acidic tundra. At the same time, there were moisture thresholds beyond which waterlogging and subsequent plant mortality drove a rapid decline in all C fluxes, similar to the results of Heiskanen et al. (2021) in a subarctic fen. We saw opposite, non-linear responses of NEE to variability in surface moisture and soil moisture; NEE first decreased then increased as variability in surface moisture increased and increased then decreased with variability in soil moisture. These patterns were less strong and harder to explain, but the differences could be due to the different depths at which those two measurements are taken (Figure S7). Surface moisture was measured in the top 5 cm of moss, and tended to be less variable than soil moisture, which was measured in the top 15 cm. Surface moisture may have been less variable than soil moisture because the moss surface typically remained dry everywhere but TK-centers, while soil moisture was measured down to the depth of the average water table in many plots, and therefore could fluctuate rapidly as the water table depth rose and fell.

4.3. Implications of Abrupt Thaw for the Future of Carbon Fluxes

The non-linear responses of GPP, R_{eco}, and NEE to experimental warming, driven by subsidence and redistribution of water (Figure 1, Figure 5), did not begin manifesting until year 4 and, in some plots, was not apparent until the last few years of this 13 year experiment. This indicates that short-term studies may miss important feedbacks that develop over longer timeframes. In fact, we suspect that flux trajectories at this site could reverse again. First, we expect that plant succession and shifting community composition, as has been observed more broadly at the site (Schuur et al., 2007), will result in greater growing season CO_2 uptake in the coming years to decades, particularly within thermokarst depressions that are currently experiencing plant mortality. Second, continued thaw will likely cause thermokarst features to expand and merge, resulting in higher hydraulic connectivity and drier soil conditions (Figure 7: ‘Advanced Thaw’)(Connon et al., 2018; Nitze et al., 2020) that would likely lead to larger CO_2 release due to the impact of drought on GPP (Schuur et al., 2021). The timing of these two processes will determine if and when flux trajectories reverse in the future.

The eventual development of drier conditions would reflect what most Earth system models (ESMs) predict in permafrost ecosystems, however these models oversimplify the processes involved in permafrost thaw and often miss the potential for divergent hydrologic conditions to develop during early stages of abrupt thaw. Many models predict that drying will occur progressively, because they do not include subsidence (Andresen et al., 2020; Lawrence et al., 2015; Schädel et al., 2018), while field studies, including ours, indicate that the trajectory of hydrology, and therefore fluxes, is not linear (Hinkel & Hurd, 2006; Jorgenson et al., 2013; Varner et al., 2022) due to differential subsidence and redistribution of water. As shown in this study, this patchwork of wet and dry conditions could persist on the landscape for years or perhaps longer (Varner et al., 2022), contrary to modeling that has predicted the transition from wet to dry conditions could take only a few months (Teufel & Sushama, 2019). Given a transition period of years to decades, and strong responses of NEE to varying environmental conditions, the impact of abrupt thaw on cumulative fluxes could be large, making it important to understand how long this transition period could take (Lawrence et al., 2015). Over a 13-year period within this upland landscape, we observed a wide variety of hydrologic responses but overall wetter conditions and plant mortality, and it is uncertain how much longer it may take before thermokarst features merge and drain or plant succession begins. Regardless of the hydrologic path, however, our results indicate that the long-term impact of abrupt permafrost thaw will be to shift tundra ecosystems towards higher annual carbon emissions, mobilizing centuries of accumulated permafrost soil carbon and accelerating climate change.

Conflict of Interest

The authors have no conflicts of interest to declare.

Figure Captions

Figure 1. Experimental warming effects on growing season NEE, R_{eco}, and GPP throughout the course of the experiment. Bar height indicates the difference in cumulative growing season flux between each treatment and the control. Error bars show the standard error. Strong treatment effects of warming in the first several years declined or reversed later in the experiment.

Figure 2. Initial (Year 1, 2009; open circles) and final (Year 13, 2021; filled circles) ALT and mean annual water table depth in the warming experiment. Each point represents one plot, with gray representing control and black representing soil warming. The dashed lines represent a water table depth of 0, or water table depth at the soil surface, and the mean ALT in year 1.

Figure 3. A) Thermokarst classification at CiPEHR in years 9 and 13 of the experiment. Non-thermokarst is shown in light gray, thermokarst-margins are shown in medium gray, and thermokarst-centers are shown in dark gray. B) Count of CiPEHR plots in each thermokarst class between year 9 and 13. C) Count of CiPEHR plots, grouped by warming treatment, in each thermokarst class between year 9 and 13.

Figure 4. Differences in environmental conditions between initial conditions, non-thermokarst, thermokarst-margins, and thermokarst-centers: A) ALT, B) surface moisture, C) standard deviation of surface moisture, D) subsidence, E) soil moisture, F) standard deviation of soil moisture, G) AG Biomass, H) water table depth, and I) standard deviation of water table depth. Gray points represent the average value for a single plot in a single year with a gray violin plot overlaid, while black points

represent the average value across all plots with black error bars representing between-plot standard deviation. Year 2 was used for initial conditions, due to disturbance from experimental set-up in years 0 and 1. Thermokarst classifications were available in years 9-13. The background shading indicates measurements made in year 2 (gray) or years 9-13 (no shading). Statistically significant differences in group means are indicated with letters. Note that increasing between-plot variability within classes makes it harder to detect differences in group means.

Figure 5. The trajectory of growing season CO_2 fluxes throughout the course of the warming experiment in each of the thermokarst classes with splines to highlight trends through time. 95% CI shown as gray bands. Each plot was assigned to the same thermokarst class in all years based on the thermokarst class in 2021. Each point represents the growing season cumulative CO_2 flux for an individual plot. Color indicates plot-level AG Biomass and shape indicates experimental treatment. Opaque points indicate growing season sums of gap-filled measurements, and transparent points in year 11 indicate growing season sums which were modeled, because the plots were not monitored.

Figure 6. The relative influence (percent reduction in sum of squared error attributable to each variable) of environmental variables included in the monthly and cumulative growing season regression tree models of GPP, NEE, and R_{eco}, with linear regressions using validation data in the insets to evaluate model fit. Validation regression slopes were calculated using geometric mean regression. Abbreviations are as follows: SD = standard deviation, GDD = growing degree days, 5-cm SM = 0-5 cm surface moisture, 15-cm SM = 0-15 cm soil moisture, WTD = water table depth, FDD = freezing degree days, ALT = active layer thickness.

Figure 7. A diagram of hydrologic conditions and CO_2 fluxes as abrupt permafrost thaw progresses. NTK refers to non-thermokarst, TM refers to hermokarstmargin, and TK refers to thermokarst-center. Initially, the permafrost table is a relatively consistent depth below the soil surface and so is water table depth (water table depth). The ecosystem is a slight carbon sink on an annual basis. During early-thaw, depressions form in the permafrost table and soil surface, causing water in the soil profile to drain from non-thermokarst areas and into the thermokarst-centers. This leads to a patchwork of subsided, wet microsites, and relatively unsubsided, dry microsites. All areas of the landscape are annual carbon sources, with the lowest source occurring in non-thermokarst areas where R_{eco} increased more than GPP, and the highest source occurring in thermokarst-centers, where GPP was suppressed more than R_{eco}. During advanced-thaw, not yet observed at this site, discrete thermokarst depressions expand and merge with nearby thermokarst features, leading to deeper permafrost table depths across the landscape and drier conditions, as the water table depth tracks the permafrost table. Permafrost ecosystems in advanced stages of thaw are likely to be carbon sources, although the magnitude is uncertain. Artwork by Victor Leshyk.

References

Abbott, B. W., & Jones, J. B. (2015). Permafrost collapse alters soil carbon stocks, respiration, CH_4, and N_2O in upland tundra. *Global Change Biology*, *21*(12), 4570–4587. https://doi.org/10.1111/gcb.13069

Andresen, C. G., Lawrence, D. M., Wilson, C. J., McGuire, A. D., Koven, C., Schaefer, K., Jafarov, E., Peng, S., Chen, X., Gouttevin, I., Burke, E., Chadburn, S., Ji, D., Chen, G., Hayes, D., & Zhang, W. (2020). Soil moisture and hydrology projections of the permafrost region – a model intercomparison. *The Cryosphere*, *14*(2), 445–459. https://doi.org/10.5194/tc-14-445-2020

Baldocchi, D., Falge, E., Gu, L., Olson, R., Hollinger, D., Running, S., Anthoni, P., Bernhofer, C., Davis, K., Evans, R., Fuentes, J., Goldstein, A., Katul, G., Law, B., Lee, X., Malhi, Y., Meyers, T., Munger, W., Oechel, W., … Wofsy, S. (2001). FLUXNET: A New Tool to Study the Temporal and Spatial Variability of Ecosystem–Scale Carbon Dioxide, Water Vapor, and Energy Flux Densities. *Bulletin of the American Meteorological Society*, *82*(11), 2415–2434. https://doi.org/10.1175/1520-0477(2001)082<2415:FANTTS>2.3.CO;2

Biskaborn, B. K., Smith, S. L., Noetzli, J., Matthes, H., Vieira, G., Streletskiy, D. A., Schoeneich, P., Romanovsky, V. E., Lewkowicz, A. G., Abramov, A., Allard, M., Boike, J., Cable, W. L., Christiansen, H. H., Delaloye, R., Diekmann, B., Drozdov, D., Etzelmüller, B., Grosse, G., … Lantuit, H. (2019). Permafrost is warming at a global scale. *Nature Communications*, *10*(1), 264. https://doi.org/10.1038/s41467-018-08240-4

Cassidy, A. E., Christen, A., & Henry, G. H. R. (2016). The effect of a permafrost disturbance on growing-season carbon-dioxide fluxes in a high Arctic tundra ecosystem. *Biogeosciences*, *13*(8), 2291–2303. https://doi.org/10.5194/bg-13-2291-2016

Celis, G., Mauritz, M., Bracho, R., Salmon, V. G., Webb, E. E., Hutchings, J., Natali, S. M., Schädel, C., Crummer, K. G., & Schuur, E. A. G. (2017). Tundra is a consistent source of CO_2 at a site with progressive permafrost thaw during 6 years of chamber and eddy covariance measurements: Tundra CO_2 Fluxes. *Journal of Geophysical Research: Biogeosciences*, *122*(6), 1471–1485. https://doi.org/10.1002/2016JG003671

Collins, C. G., Elmendorf, S. C., Hollister, R. D., Henry, G. H. R., Clark, K., Bjorkman, A. D., Myers-Smith, I. H., Prevéy, J. S., Ashton, I. W., Assmann, J. J., Alatalo, J. M., Carbognani, M., Chisholm, C., Cooper, E. J., Forrester, C., Jónsdóttir, I. S., Klanderud, K., Kopp, C. W., Livensperger, C., … Suding, K. N. (2021). Experimental warming differentially affects vegetative and reproductive phenology of tundra plants. *Nature Communications*, *12*(1), 3442. https://doi.org/10.1038/s41467-021-23841-2

Connon, R., Devoie, É., Hayashi, M., Veness, T., & Quinton, W. (2018). The Influence of Shallow Taliks on Permafrost Thaw and Active Layer Dynamics in Subarctic Canada. *Journal of*

Geophysical Research: Earth Surface, *123*(2), 281–297. https://doi.org/10.1002/2017JF004469

Deane-Coe, K. K., Mauritz, M., Celis, G., Salmon, V., Crummer, K. G., Natali, S. M., & Schuur, E. A. G. (2015). Experimental Warming Alters Productivity and Isotopic Signatures of Tundra Mosses. *Ecosystems*, *18*(6), 1070–1082. https://doi.org/10.1007/s10021-015-9884-7

Dowle, M., & Srinivasan, A. (2021). *data.table: Extension of `data.frame`*. (1.14.0) [R]. https://CRAN.R-project.org/package=data.table

Ekici, A., Lee, H., Lawrence, D. M., Swenson, S. C., & Prigent, C. (2019). Ground subsidence effects on simulating dynamic high-latitude surface inundation under permafrost thaw using CLM5. *Geoscientific Model Development*, *12*(12), 5291–5300. https://doi.org/10.5194/gmd-12-5291-2019

Elzhov, T. V., Mullen, K. M., Spiess, A.-N., & Bolker, B. M. (2016). *minpack.lm: R interface to the Levenberg-Marquardt nonlinear least-squares algorithm found in MINPACK, plus support for bounds* (1.2-1) [R]. https://CRAN.R-project.org/package=minpack.lm

Emmerton, C. A., St. Louis, V. L., Humphreys, E. R., Gamon, J. A., Barker, J. D., & Pastorello, G. Z. (2016). Net ecosystem exchange of CO_2 with rapidly changing high Arctic landscapes. *Global Change Biology*, *22*(3), 1185–1200. https://doi.org/10.1111/gcb.13064

Euskirchen, E. S., Edgar, C. W., Syndonia Bret-Harte, M., Kade, A., Zimov, N., & Zimov, S. (2017). Interannual and seasonal patterns of carbon dioxide, water, and energy fluxes from ecotonal and thermokarst-impacted ecosystems on carbon-rich permafrost soils in northeastern Siberia. *Journal of Geophysical Research: Biogeosciences*, *122*(10), 2651–2668. https://doi.org/10.1002/2017JG004070

Evans, S. G., Godsey, S. E., Rushlow, C. R., & Voss, C. (2020). Water Tracks Enhance Water Flow Above Permafrost in Upland Arctic Alaska Hillslopes. *Journal of Geophysical Research: Earth Surface*, *125*(2). https://doi.org/10.1029/2019JF005256

Farquharson, L. M., Romanovsky, V. E., Cable, W. L., Walker, D. A., Kokelj, S. V., & Nicolsky, D.

(2019). Climate change drives widespread and rapid thermokarst development in very cold permafrost in the Canadian high Arctic. *Geophysical Research Letters*, *46*(12), 6681–6689. https://doi.org/10.1029/2019GL082187

Greenwell, B., Boehmke, B., Cunningham, J., & GBM Developers. (2020). *gbm: Generalized boosted regression models* (2.1.8) [R]. https://CRAN.R-project.org/package=gbm

Harris, S. A., French, H. M., Hegginbottom, J. A., Johnston, G. H., Ladanyi, B., Sego, D. C., & van Everdingen, R. O. (1988). *Glossary of permafrost and related ground-ice terms* (Technical Memorandum (National Research Council of Canada. Associate Committee on Geotechnical Research), No. ACGR-TM-142., p. 159). National Research Council of Canada. Associate Committee on Geotechnical Research. Permafrost Subcommittee. https://doi.org/10.4224/20386561

Heiskanen, L., Tuovinen, J.-P., Räsänen, A., Virtanen, T., Juutinen, S., Lohila, A., Penttilä, T., Linkosalmi, M., Mikola, J., Laurila, T., & Aurela, M. (2021). Carbon dioxide and methane exchange of a patterned subarctic fen during two contrasting growing seasons. *Biogeosciences*, *18*(3), 873–896. https://doi.org/10.5194/bg-18-873-2021

Hewitt, R. E., Taylor, D. L., Genet, H., McGuire, A. D., & Mack, C. (2018). *Below-ground plant traits influence tundra plant acquisition of newly thawed permafrost nitrogen*. 13.

Hicks Pries, C. E., Schuur, E. A. G., & Crummer, K. G. (2013). Thawing permafrost increases old soil and autotrophic respiration in tundra: Partitioning ecosystem respiration using δ^{13}C and Δ^{14}C. *Global Change Biology*, *19*(2), 649–661. https://doi.org/10.1111/gcb.12058

Hiemstra, P. H., Pebesma, E., Twenhöfel, C. J. W., & Heuvelink, G. B. M. (2009). *Real-time automatic interpolation of ambient gamma dose rates from the Dutch Radioactivity Monitoring Network*. *35*(8), 1711–1721.

Hinkel, K. M., & Hurd, J. K. (2006). Permafrost Destabilization and Thermokarst Following Snow Fence Installation, Barrow, Alaska, U.S.A. *Arctic, Antarctic, and Alpine Research*, *38*(4), 530–

539. https://doi.org/10.1657/1523-0430(2006)38[530:PDATFS]2.0.CO;2

Houghton, R. A. (2007). Balancing the global carbon budget. *Annual Review of Earth and Planetary Sciences*, *35*, 313–347.

Hugelius, G., Strauss, J., Zubrzycki, S., Harden, J. W., Schuur, E. A. G., Ping, C.-L., Schirrmeister, L., Grosse, G., Michaelson, G. J., Koven, C. D., O'Donnell, J. A., Elberling, B., Mishra, U., Camill, P., Yu, Z., Palmtag, J., & Kuhry, P. (2014). Estimated stocks of circumpolar permafrost carbon with quantified uncertainty ranges and identified data gaps. *Biogeosciences*, *11*(23), 6573–6593. https://doi.org/10.5194/bg-11-6573-2014

Huxman, T. E., Turnipseed, A. A., Sparks, J. P., Harley, P. C., & Monson, R. K. (2003). Temperature as a control over ecosystem CO_2 fluxes in a high-elevation, subalpine forest. *Oecologia*, *134*(4), 537–546. https://doi.org/10.1007/s00442-002-1131-1

IPCC. (2021). *Climate Change 2021: The Physical Science Basis. Contribution of Working Group I to the Sixth Assessment Report of the Intergovernmental Panel on Climate Change*. Cambridge University Press.

Jensen, A. E., Lohse, K. A., Crosby, B. T., & Mora, C. I. (2014). Variations in soil carbon dioxide efflux across a thaw slump chronosequence in northwestern Alaska. *Environmental Research Letters*, *9*(2), 025001. https://doi.org/10.1088/1748-9326/9/2/025001

Jorgenson, M. T., Douglas, T. A., Liljedahl, A. K., Roth, J. E., Cater, T. C., Davis, W. A., Frost, G. V., Miller, P. F., & Racine, C. H. (2020). The roles of climate extremes, ecological succession, and hydrology in repeated permafrost aggradation and degradation in fens on the Tanana Flats, Alaska. *Journal of Geophysical Research: Biogeosciences*, *125*(12). https://doi.org/10.1029/2020JG005824

Jorgenson, M. T., Harden, J., Kanevskiy, M., O'Donnell, J., Wickland, K., Ewing, S., Manies, K., Zhuang, Q., Shur, Y., Striegl, R., & Koch, J. (2013). Reorganization of vegetation, hydrology and soil carbon after permafrost degradation across heterogeneous boreal landscapes.

Environmental Research Letters, *8*(3), 035017. https://doi.org/10.1088/1748-9326/8/3/035017

Jorgenson, M. T., & Osterkamp, T. E. (2005). Response of boreal ecosystems to varying modes of permafrost degradation. *Canadian Journal of Forest Research*, *35*, 2100–2111. https://doi.org/10.1139/X05-153

Jorgenson, M. T., Racine, C. H., Walters, J. C., & Osterkamp, T. E. (2001). Permafrost Degradation and Ecological Changes Associated with a WarmingClimate in Central Alaska. *Climatic Change*, *48*, 551–579.

Jorgenson, M. T., Shur, Y. L., & Pullman, E. R. (2006). Abrupt increase in permafrost degradation in Arctic Alaska. *Geophysical Research Letters*, *33*(2), L02503. https://doi.org/10.1029/2005GL024960

Kanevskiy, M., Shur, Y., Jorgenson, T., Brown, D. R. N., Moskalenko, N., Brown, J., Walker, D. A., Raynolds, M. K., & Buchhorn, M. (2017). Degradation and stabilization of ice wedges: Implications for assessing risk of thermokarst in northern Alaska. *Geomorphology*, *297*, 20–42. https://doi.org/10.1016/j.geomorph.2017.09.001

Kelsey, K. C., Pedersen, S. H., Leffler, A. J., Sexton, J. O., Feng, M., & Welker, J. M. (2021). Winter snow and spring temperature have differential effects on vegetation phenology and productivity across Arctic plant communities. *Global Change Biology*, *27*(8), 1572–1586. https://doi.org/10.1111/gcb.15505

Köchy, M., Hiederer, R., & Freibauer, A. (2015). Global distribution of soil organic carbon – Part 1: Masses and frequency distributions of SOC stocks for the tropics, permafrost regions, wetlands, and the world. *SOIL*, *1*(1), 351–365. https://doi.org/10.5194/soil-1-351-2015

Kokelj, S. V., & Jorgenson, M. T. (2013). Advances in thermokarst research: Recent advances in research investigating thermokarst processes. *Permafrost and Periglacial Processes*, *24*(2), 108–119. https://doi.org/10.1002/ppp.1779

Kotani, A., Saito, A., Kononov, A. V., Petrov, R. E., Maximov, T. C., Iijima, Y., & Ohta, T. (2019).

Impact of unusually wet permafrost soil on understory vegetation and CO_2 exchange in a larch forest in eastern Siberia. *Agricultural and Forest Meteorology*, *265*, 295–309. https://doi.org/10.1016/j.agrformet.2018.11.025

Kuhn, M. (2021). *caret: Classification and regression training* (6.0-90) [R]. https://CRAN.R-project.org/package=caret

Lantz, T. C., & Kokelj, S. V. (2008). Increasing rates of retrogressive thaw slump activity in the Mackenzie Delta region, N.W.T., Canada. *Geophysical Research Letters*, *35*(6), L06502. https://doi.org/10.1029/2007GL032433

Lara, M. J., Genet, H., McGuire, A. D., Euskirchen, E. S., Zhang, Y., Brown, D. R. N., Jorgenson, M. T., Romanovsky, V., Breen, A., & Bolton, W. R. (2016). Thermokarst rates intensify due to climate change and forest fragmentation in an Alaskan boreal forest lowland. *Global Change Biology*, *22*(2), 816–829. https://doi.org/10.1111/gcb.13124

Lawrence, D. M., Koven, C. D., Swenson, S. C., Riley, W. J., & Slater, A. G. (2015). Permafrost thaw and resulting soil moisture changes regulate projected high-latitude CO_2 and CH_4 emissions. *Environmental Research Letters*, *10*(9), 094011. https://doi.org/10.1088/1748-9326/10/9/094011

Lee, H., Schuur, E. A. G., Vogel, J. G., Lavoie, M., Bhadra, D., & Staudhammer, C. L. (2011). A spatially explicit analysis to extrapolate carbon fluxes in upland tundra where permafrost is thawing. *Global Change Biology*, *17*(3), 1379–1393. https://doi.org/10.1111/j.1365-2486.2010.02287.x

Lee, H., Swenson, S. C., Slater, A. G., & Lawrence, D. M. (2014). Effects of excess ground ice on projections of permafrost in a warming climate. *Environmental Research Letters*, *9*(12), 124006. https://doi.org/10.1088/1748-9326/9/12/124006

Luo, D., Wu, Q., Jin, H., Marchenko, S. S., Lü, L., & Gao, S. (2016). Recent changes in the active layer thickness across the northern hemisphere. *Environmental Earth Sciences*, *75*(7), 555.

https://doi.org/10.1007/s12665-015-5229-2

Mauritz, M., Bracho, R., Celis, G., Hutchings, J., Natali, S. M., Pegoraro, E., Salmon, V. G., Schädel, C., Webb, E. E., & Schuur, E. A. G. (2017). Nonlinear CO_2 flux response to 7 years of experimentally induced permafrost thaw. *Global Change Biology*, *23*(9), 3646–3666. https://doi.org/10.1111/gcb.13661

Meredith, M., SommerKorn, M., Cassota, S., Derksen, C., Ekaykin, A., Hallowed, A., Kofinas, G., Mackintosh, A., Melbourne-Thomas, J., Muelbert, M. M. C., Ottersen, G., Pritchard, H., Schuur, E. A. G., Boyd, P., & Hobbs, W. (2019). Polar Regions. In H.-O. Pörtner, D. C. Roberts, V. Masson-Delmotte, P. Zhai, M. Tignor, E. Poloczanska, K. Mintenbeck, A. Alegría, M. Nicolai, A. Okem, J. Petzold, B. Rama, & N. M. Weyer (Eds.), *IPCC Special Report on the Ocean and Cryosphere in a Changing Climate*.

Miner, K. R., Turetsky, M. R., Malina, E., Bartsch, A., Tamminen, J., McGuire, A. D., Fix, A., Sweeney, C., Elder, C. D., & Miller, C. E. (2022). Permafrost carbon emissions in a changing Arctic. *Nature Reviews Earth & Environment*, *3*(1), 55–67. https://doi.org/10.1038/s43017-021-00230-3

Mishra, U., Hugelius, G., Shelef, E., Yang, Y., Strauss, J., Lupachev, A., Harden, J. W., Jastrow, J. D., Ping, C.-L., Riley, W. J., Schuur, E. A. G., Matamala, R., Siewert, M., Nave, L. E., Koven, C. D., Fuchs, M., Palmtag, J., Kuhry, P., Treat, C. C., … Orr, A. (2021). Spatial heterogeneity and environmental predictors of permafrost region soil organic carbon stocks. *Science Advances*, *7*(9), eaaz5236. https://doi.org/10.1126/sciadv.aaz5236

Natali, S. M., Holdren, J. P., Rogers, B. M., Treharne, R., Duffy, P. B., Pomerance, R., & MacDonald, E. (2021). Permafrost carbon feedbacks threaten global climate goals. *Proceedings of the National Academy of Sciences*, *118*(21), e2100163118. https://doi.org/10.1073/pnas.2100163118

Natali, S. M., Schuur, E. A. G., Mauritz, M., Schade, J. D., Celis, G., Crummer, K. G., Johnston, C., Krapek, J., Pegoraro, E., Salmon, V. G., & Webb, E. E. (2015). Permafrost thaw and soil moisture driving CO_2 and CH_4 release from upland tundra. *Journal of Geophysical Research: Biogeosciences*, *120*(3), 525–537. https://doi.org/10.1002/2014JG002872

Natali, S. M., Schuur, E. A. G., Trucco, C., Hicks Pries, C. E., Crummer, K. G., & Baron Lopez, A. F. (2011). Effects of experimental warming of air, soil and permafrost on carbon balance in Alaskan tundra. *Global Change Biology*, *17*(3), 1394–1407. https://doi.org/10.1111/j.1365-2486.2010.02303.x

Natali, S. M., Watts, J. D., Rogers, B. M., Potter, S., Ludwig, S. M., Selbmann, A.-K., Sullivan, P. F., Abbott, B. W., Arndt, K. A., Birch, L., Björkman, M. P., Bloom, A. A., Celis, G., Christensen, T. R., Christiansen, C. T., Commane, R., Cooper, E. J., Crill, P., Czimczik, C., … Zona, D. (2019). Large loss of CO_2 in winter observed across the northern permafrost region. *Nature Climate Change*, *9*(11), 852–857. https://doi.org/10.1038/s41558-019-0592-8

NEON (National Ecological Observatory Network). (2022). *Elevation—LiDAR, RELEASE-2020 (DP3.30024.001)*. https://doi.org/10.48443/917d-g459

Nitze, I., Cooley, S. W., Duguay, C. R., Jones, B. M., & Grosse, G. (2020). The catastrophic thermokarst lake drainage events of 2018 in northwestern Alaska: Fast-forward into the future. *The Cryosphere*, *14*(12), 4279–4297. https://doi.org/10.5194/tc-14-4279-2020

Niu, S., Luo, Y., Fei, S., Montagnani, L., Bohrer, G., Janssens, I. A., Gielen, B., Rambal, S., Moors, E., & Matteucci, G. (2011). Seasonal hysteresis of net ecosystem exchange in response to temperature change: Patterns and causes. *Global Change Biology*, *17*(10), 3102–3114. https://doi.org/10.1111/j.1365-2486.2011.02459.x

Nyland, K. E., Shiklomanov, N. I., Streletskiy, D. A., Nelson, F. E., Klene, A. E., & Kholodov, A. L. (2021). Long-term Circumpolar Active Layer Monitoring (CALM) program observations in Northern Alaskan tundra. *Polar Geography*, 1–19. https://doi.org/10.1080/1088937X.2021.1988000

Olefeldt, D., Goswami, S., Grosse, G., Hayes, D., Hugelius, G., Kuhry, P., McGuire, A. D., Romanovsky, V. E., Sannel, A. B. K., Schuur, E. A. G., & Turetsky, M. R. (2016). Circumpolar distribution and carbon storage of thermokarst landscapes. *Nature Communications*, *7*(1), 13043. https://doi.org/10.1038/ncomms13043

Osterkamp, T. E., Jorgenson, M. T., Schuur, E. A. G., Shur, Y. L., Kanevskiy, M. Z., Vogel, J. G., & Tumskoy, V. E. (2009). Physical and ecological changes associated with warming permafrost and thermokarst in Interior Alaska. *Permafrost and Periglacial Processes*, *20*(3), 235–256. https://doi.org/10.1002/ppp.656

Ping, C. L., Jastrow, J. D., Jorgenson, M. T., Michaelson, G. J., & Shur, Y. L. (2015). Permafrost soils and carbon cycling. *SOIL*, *1*(1), 147–171. https://doi.org/10.5194/soil-1-147-2015

R Core Team. (2021). *R: A language and environment for statistical computing* (4.1.0) [Computer software]. R Foundation for Statistical Computing. https://www.R-project.org/

Rantanen, M., Karpechko, A. Yu., Lipponen, A., Nordling, K., Hyvärinen, O., Ruosteenoja, K., Vihma, T., & Laaksonen, A. (2022). The Arctic has warmed nearly four times faster than the globe since 1979. *Communications Earth & Environment*, *3*(1), 168. https://doi.org/10.1038/s43247-022-00498-3

Rodenhizer, H., Belshe, F., Celis, G., Ledman, J., Mauritz, M., Goetz, S., Sankey, T., & Schuur, E. A. G. (2022). Abrupt permafrost thaw accelerates carbon dioxide and methane release at a tussock tundra site. *Arctic, Antarctic, and Alpine Research*, *54*(1), 443–464. https://doi.org/10.1080/15230430.2022.2118639

Rodenhizer, H., Ledman, J., Mauritz, M., Natali, S. M., Pegoraro, E., Plaza, C., Romano, E., Schädel, C., Taylor, M., & Schuur, E. (2020). Carbon thaw rate doubles when accounting for subsidence in a permafrost warming experiment. *Journal of Geophysical Research: Biogeosciences*, *125*(6). https://doi.org/10.1029/2019JG005528

Romanovsky, V. E., Smith, S. L., & Christiansen, H. H. (2010). Permafrost thermal state in the polar

Northern Hemisphere during the international polar year 2007-2009: A synthesis. *Permafrost and Periglacial Processes*, *21*(2), 106–116. https://doi.org/10.1002/ppp.689

Salmon, V. G., Soucy, P., Mauritz, M., Celis, G., Natali, S. M., Mack, M. C., & Schuur, E. A. G. (2016). Nitrogen availability increases in a tundra ecosystem during five years of experimental permafrost thaw. *Global Change Biology*, *22*(5), 1927–1941. https://doi.org/10.1111/gcb.13204

Schädel, C., Bader, M. K.-F., Schuur, E. A. G., Biasi, C., Bracho, R., Čapek, P., De Baets, S., Diáková, K., Ernakovich, J., Estop-Aragones, C., Graham, D. E., Hartley, I. P., Iversen, C. M., Kane, E., Knoblauch, C., Lupascu, M., Martikainen, P. J., Natali, S. M., Norby, R. J., … Wickland, K. P. (2016). Potential carbon emissions dominated by carbon dioxide from thawed permafrost soils. *Nature Climate Change*, *6*(10), 950–953. https://doi.org/10.1038/nclimate3054

Schädel, C., Koven, C. D., Lawrence, D. M., Celis, G., Garnello, A. J., Hutchings, J., Mauritz, M., Natali, S. M., Pegoraro, E., Rodenhizer, H., Salmon, V. G., Taylor, M. A., Webb, E. E., Wieder, W. R., & Schuur, E. A. (2018). Divergent patterns of experimental and model-derived permafrost ecosystem carbon dynamics in response to Arctic warming. *Environmental Research Letters*, *13*(10), 105002. https://doi.org/10.1088/1748-9326/aae0ff

Schuur, E. A. G., & Abbott, B. (2011). High risk of permafrost thaw. *Nature*, *480*(7375), 32–33. https://doi.org/10.1038/480032a

Schuur, E. A. G., Abbott, B. W., Commane, R., Ernakovich, J., Euskirchen, E., Hugelius, G., Grosse, G., Jones, M., Koven, C., Leshyk, V., Lawrence, D., Loranty, M. M., Mauritz, M., Olefeldt, D., Natali, S., Rodenhizer, H., Salmon, V., Schädel, C., Strauss, J., … Turetsky, M. (2022). *Permafrost and Climate Change: Carbon Cycle Feedbacks From the Warming Arctic*. 33.

Schuur, E. A. G., Bockheim, J., Canadell, J. G., Euskirchen, E., Field, C. B., Goryachkin, S. V., Hagemann, S., Kuhry, P., Lafleur, P. M., Lee, H., Mazhitova, G., Nelson, F. E., Rinke, A., Romanovsky, V. E., Shiklomanov, N., Tarnocai, C., Venevsky, S., Vogel, J. G., & Zimov, S. A. (2008). Vulnerability of permafrost carbon to climate change: Implications for the global carbon cycle. *BioScience*, *58*(8), 701–714. https://doi.org/10.1641/B580807

Schuur, E. A. G., Bracho, R., Celis, G., Belshe, E. F., Ebert, C., Ledman, J., Mauritz, M., Pegoraro, E. F., Plaza, C., Rodenhizer, H., Romanovsky, V., Schädel, C., Schirokauer, D., Taylor, M., Vogel, J. G., & Webb, E. E. (2021). Tundra underlain by thawing permafrost persistently emits carbon to the atmosphere over 15 years of measurements. *Journal of Geophysical Research: Biogeosciences*, *126*(6). https://doi.org/10.1029/2020JG006044

Schuur, E. A. G., Crummer, K. G., Vogel, J. G., & Mack, M. C. (2007). Plant species composition and productivity following permafrost thaw and thermokarst in Alaskan tundra. *Ecosystems*, *10*(2), 280–292. https://doi.org/10.1007/s10021-007-9024-0

Schuur, E. A. G., & Mack, M. C. (2018). Ecological response to permafrost thaw and consequences for local and global ecosystem services. *Annual Review of Ecology, Evolution, and Systematics*, *49*(1), 279–301. https://doi.org/10.1146/annurev-ecolsys-121415-032349

Schuur, E. A. G., McGuire, A. D., Romanovsky, V. E., Schädel, C., & Mack, M. C. (2018). Arctic and boreal carbon. In N. Cavallaro, G. Shrestha, R. Birdsey, M. A. Mayes, R. G. Najjar, S. C. Reed, P. Romero-Lankao, & Z. Zhu (Eds.), *Second State of the Carbon Cycle Report (SOCCR2): A Sustained Assessment Report* (pp. 428–468). U.S. Global Change Research Program. https://doi.org/10.7930/ SOCCR2.2018.Ch11

Schuur, E. A. G., Vogel, J. G., Crummer, K. G., Lee, H., Sickman, J. O., & Osterkamp, T. E. (2009). The effect of permafrost thaw on old carbon release and net carbon exchange from tundra. *Nature*, *459*(7246), 556–559. https://doi.org/10.1038/nature08031

Subin, Z. M., Koven, C. D., Riley, W. J., Torn, M. S., Lawrence, D. M., & Swenson, S. C. (2013). Effects of Soil Moisture on the Responses of Soil Temperatures to Climate Change in Cold Regions. *JOURNAL OF CLIMATE*, *26*, 21.

Swanson, D. K. (2021). Permafrost thaw-related slope failures in Alaska's Arctic National Parks, *c*. 1980–2019. *Permafrost and Periglacial Processes*, ppp.2098. https://doi.org/10.1002/ppp.2098

Taylor, M., Celis, G., Ledman, J., Mauritz, M., Natali, S. M., Pegoraro, E., Schädel, C., & Schuur, E. A. G. (2021). Experimental soil warming and permafrost thaw increase CH_4 emissions in an upland tundra ecosystem. *JGR Biogeosciences*.

Teufel, B., & Sushama, L. (2019). Abrupt changes across the Arctic permafrost region endanger northern development. *Nature Climate Change*, *9*(11), 858–862. https://doi.org/10.1038/s41558-019-0614-6

Turetsky, M. R., Abbott, B. W., Jones, M. C., Anthony, K. W., Olefeldt, D., Schuur, E. A. G., Grosse, G., Kuhry, P., Hugelius, G., Koven, C., Lawrence, D. M., Gibson, C., Sannel, A. B. K., & McGuire, A. D. (2020). Carbon release through abrupt permafrost thaw. *Nature Geoscience*, *13*(2), 138–143. https://doi.org/10.1038/s41561-019-0526-0

Varner, R. K., Crill, P. M., Frolking, S., McCalley, C. K., Burke, S. A., Chanton, J. P., Holmes, M. E., Isogenie Project Coordinators, Saleska, S., & Palace, M. W. (2022). Permafrost thaw driven changes in hydrology and vegetation cover increase trace gas emissions and climate forcing in Stordalen Mire from 1970 to 2014. *Philosophical Transactions of the Royal Society A: Mathematical, Physical and Engineering Sciences*, *380*(2215), 20210022. https://doi.org/10.1098/rsta.2021.0022

Veremeeva, A., Nitze, I., Günther, F., Grosse, G., & Rivkina, E. (2021). Geomorphological and climatic drivers of thermokarst lake area increase trend (1999–2018) in the Kolyma Lowland Yedoma Region, North-Eastern Siberia. *Remote Sensing*, *13*(2), 178. https://doi.org/10.3390/rs13020178

Vogel, J., Schuur, E. A. G., Trucco, C., & Lee, H. (2009). Response of CO_2 exchange in a tussock tundra ecosystem to permafrost thaw and thermokarst development. *Journal of Geophysical Research*, *114*(G4), G04018. https://doi.org/10.1029/2008JG000901

Walvoord, M. A., & Kurylyk, B. L. (2016). Hydrologic Impacts of Thawing Permafrost-A Review. *Vadose Zone Journal*, *15*(6), vzj2016.01.0010. https://doi.org/10.2136/vzj2016.01.0010

Ward Jones, M. K., Pollard, W. H., & Jones, B. M. (2019). Rapid initialization of retrogressive thaw slumps in the Canadian high Arctic and their response to climate and terrain factors. *Environmental Research Letters*, *14*(5), 055006. https://doi.org/10.1088/1748-9326/ab12fd

Webb, E. E., Schuur, E. A. G., Natali, S. M., Oken, K. L., Bracho, R., Krapek, J. P., Risk, D., & Nickerson, N. R. (2016). Increased wintertime CO_2 loss as a result of sustained tundra warming: Tundra Wintertime CO_2 Loss. *Journal of Geophysical Research: Biogeosciences*, *121*(2), 249–265. https://doi.org/10.1002/2014JG002795

Wickham, H., Averick, M., Bryan, J., Chang, W., McGowan, L., François, R., Grolemund, G., Hayes, A., Henry, L., Hester, J., Kuhn, M., Pedersen, T., Miller, E., Bache, S., Müller, K., Ooms, J., Robinson, D., Seidel, D., Spinu, V., … Yutani, H. (2019). Welcome to the Tidyverse. *Journal of Open Source Software*, *4*(43), 1686. https://doi.org/10.21105/joss.01686

Zona, D., Lafleur, P. M., Hufkens, K., Gioli, B., Bailey, B., Burba, G., Euskirchen, E. S., Watts, J. D., Arndt, K. A., Farina, M., Kimball, J. S., Heimann, M., Göckede, M., Pallandt, M., Christensen, T. R., Mastepanov, M., López-Blanco, E., Dolman, A. J., Commane, R., … Oechel, W. C. (2023). Pan-Arctic soil moisture control on tundra carbon sequestration and plant productivity. *Global Change Biology*, *29*(5), 1267–1281. https://doi.org/10.1111/gcb.16487

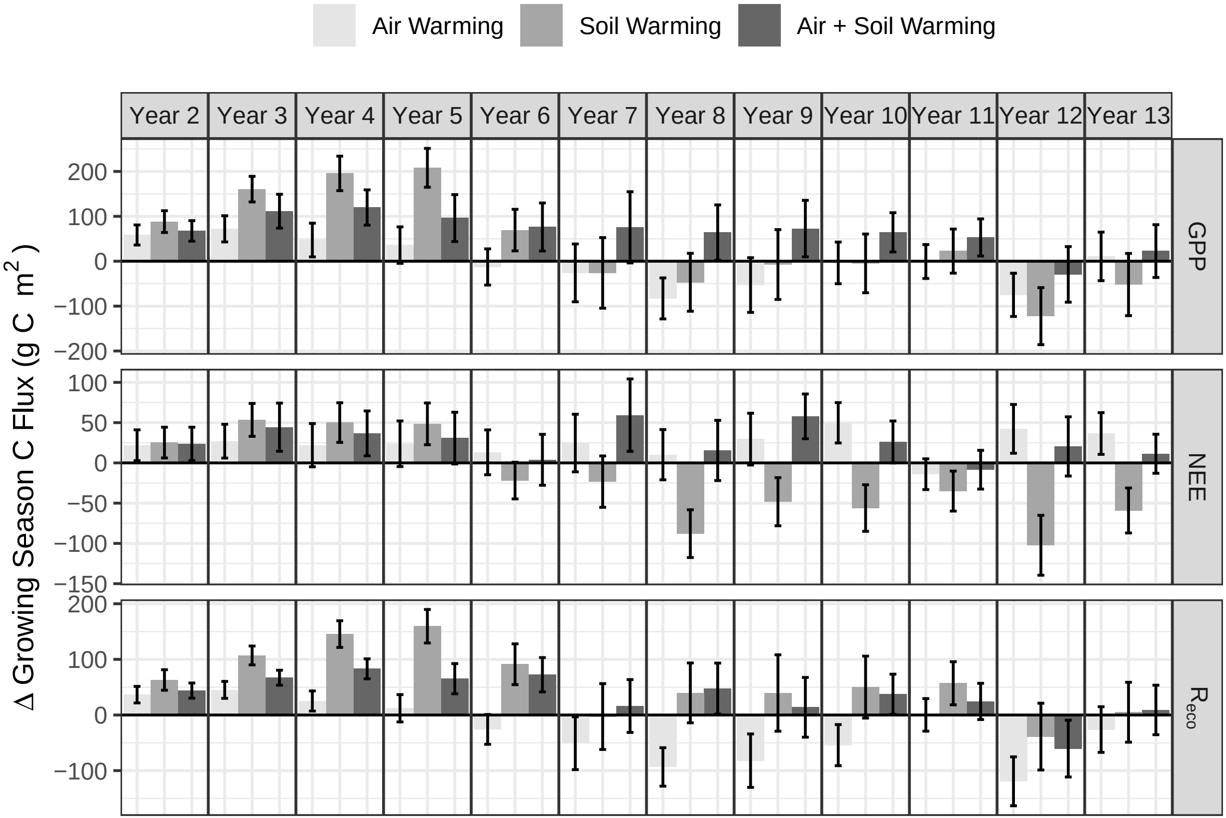
Air Warming
Soil Warming
Air + Soil Warming
Year 2
Year 3
Year 4
Year 5
Year 6
Year 7
Year 8
Year 9
Year 10
Year 11
Year 12
Year 13
GPP
NEE
R_{eco}
Δ Growing Season C Flux (g C m^{-2})
200
100
0
−100
−200
100
50
0
−50
−100
−150
200
100
0
−100

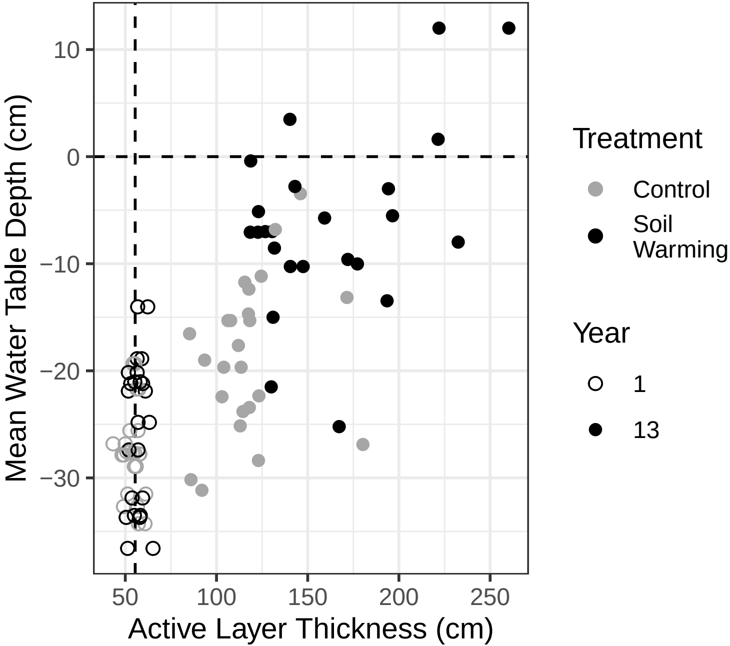

Mean Water Table Depth (cm)
10
0
−10
−20
−30
Active Layer Thickness (cm)
50
100
150
200
250
Treatment
Control
Soil Warming
Year
1
13

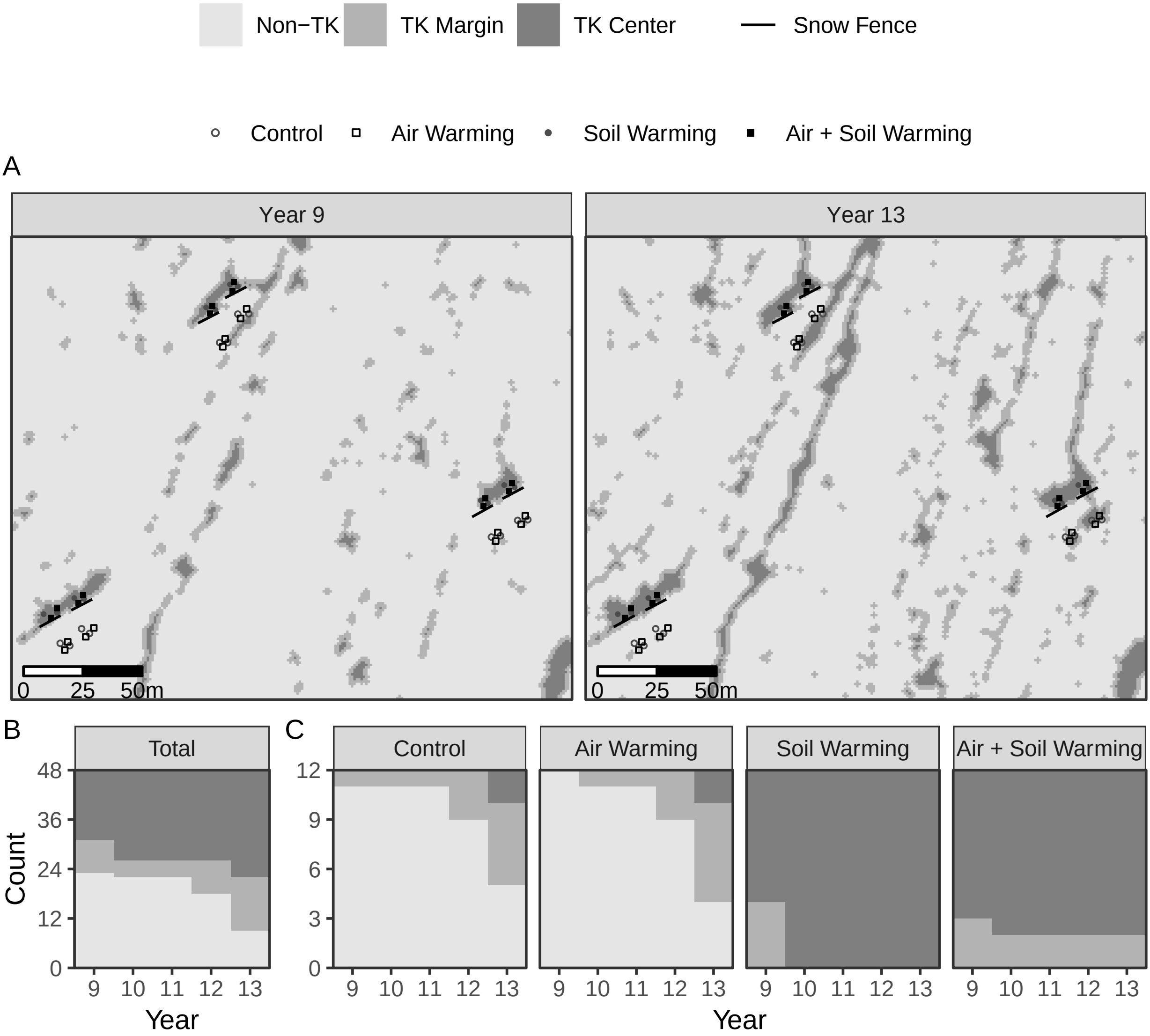
Non−TK
TK Margin
TK Center
Snow Fence
Control
Air Warming
Soil Warming
Air + Soil Warming
A
Year 9
Year 13
0
25
50m
B
Total
C
Control
Air Warming
Soil Warming
Air + Soil Warming
Count
48
36
24
12
0
12
9
6
3
0
9
10
11
12
13
Year

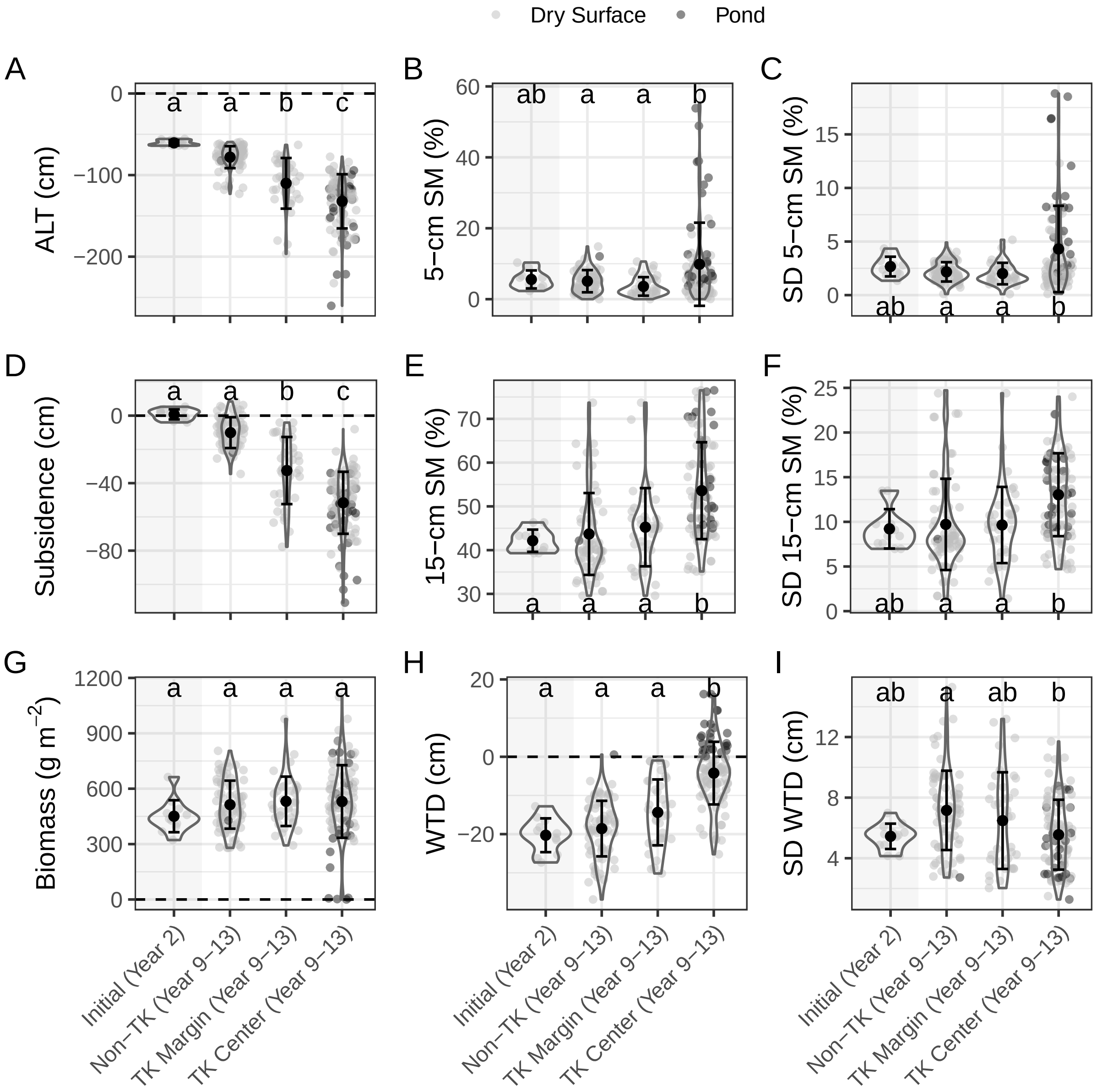
Dry Surface
Pond
A
ALT (cm)
0
−100
−200
a a b c
B
5−cm SM (%)
60
40
20
0
ab a a b
C
SD 5−cm SM (%)
15
10
5
0
ab a a b
D
Subsidence (cm)
0
−40
−80
a a b c
E
15−cm SM (%)
70
60
50
40
30
a a a b
F
SD 15−cm SM (%)
25
20
15
10
5
0
ab a a b
G
Biomass (g m^{-2})
1200
900
600
300
0
a a a a
H
WTD (cm)
20
0
−20
a a a b
I
SD WTD (cm)
12
8
4
ab a ab b
Initial (Year 2)
Non−TK (Year 9−13)
TK Margin (Year 9−13)
TK Center (Year 9−13)

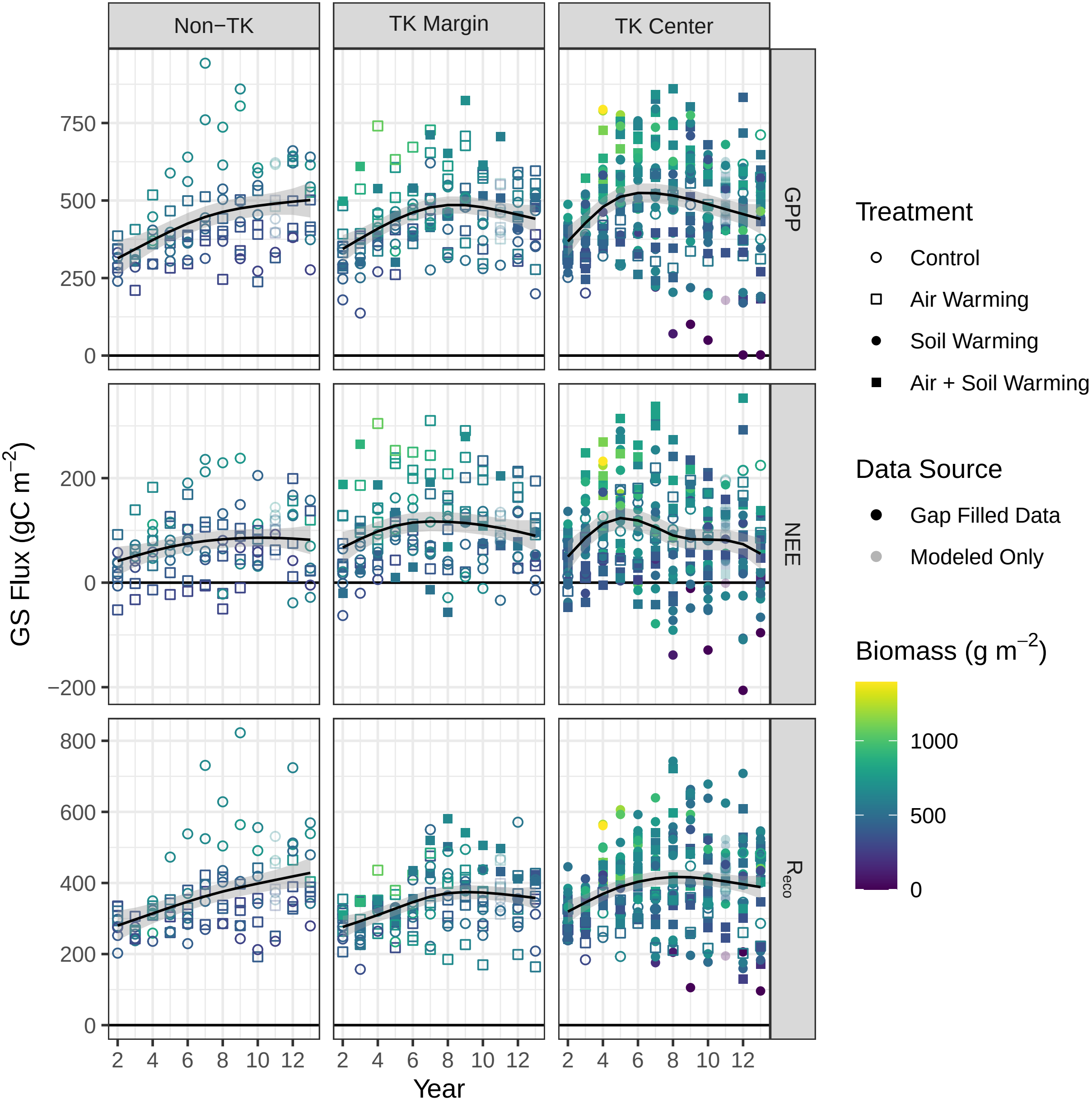
Non−TK
TK Margin
TK Center
GPP
NEE
R_{eco}
GS Flux (gC m^{-2})
Year
750
500
250
0
200
0
−200
800
600
400
200
0
2
4
6
8
10
12
Treatment
Control
Air Warming
Soil Warming
Air + Soil Warming
Data Source
Gap Filled Data
Modeled Only
Biomass (g m^{-2})
1000
500
0

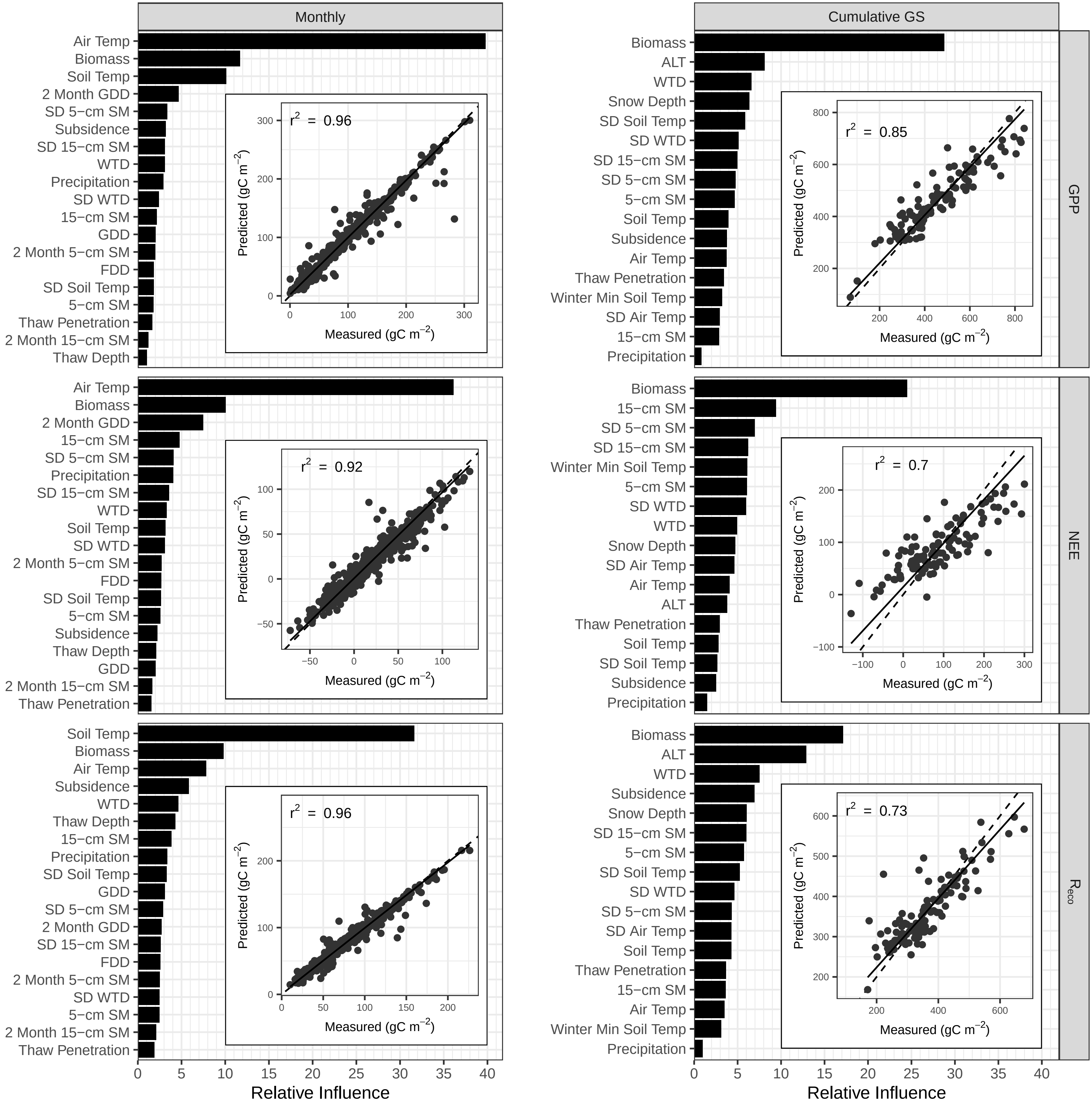
Monthly
Cumulative GS
GPP
NEE
R_{eco}
Air Temp
Biomass
Soil Temp
2 Month GDD
SD 5−cm SM
Subsidence
SD 15−cm SM
WTD
Precipitation
SD WTD
15−cm SM
GDD
2 Month 5−cm SM
FDD
SD Soil Temp
5−cm SM
Thaw Penetration
2 Month 15−cm SM
Thaw Depth
r^2 = 0.96
r^2 = 0.92
r^2 = 0.96
Biomass
ALT
WTD
Snow Depth
SD Soil Temp
SD WTD
SD 15−cm SM
SD 5−cm SM
5−cm SM
Soil Temp
Subsidence
Air Temp
Thaw Penetration
Winter Min Soil Temp
SD Air Temp
15−cm SM
Precipitation
r^2 = 0.85
r^2 = 0.7
r^2 = 0.73
Predicted (gC m^{-2})
Measured (gC m^{-2})
Relative Influence
0
5
10
15
20
25
30
35
40

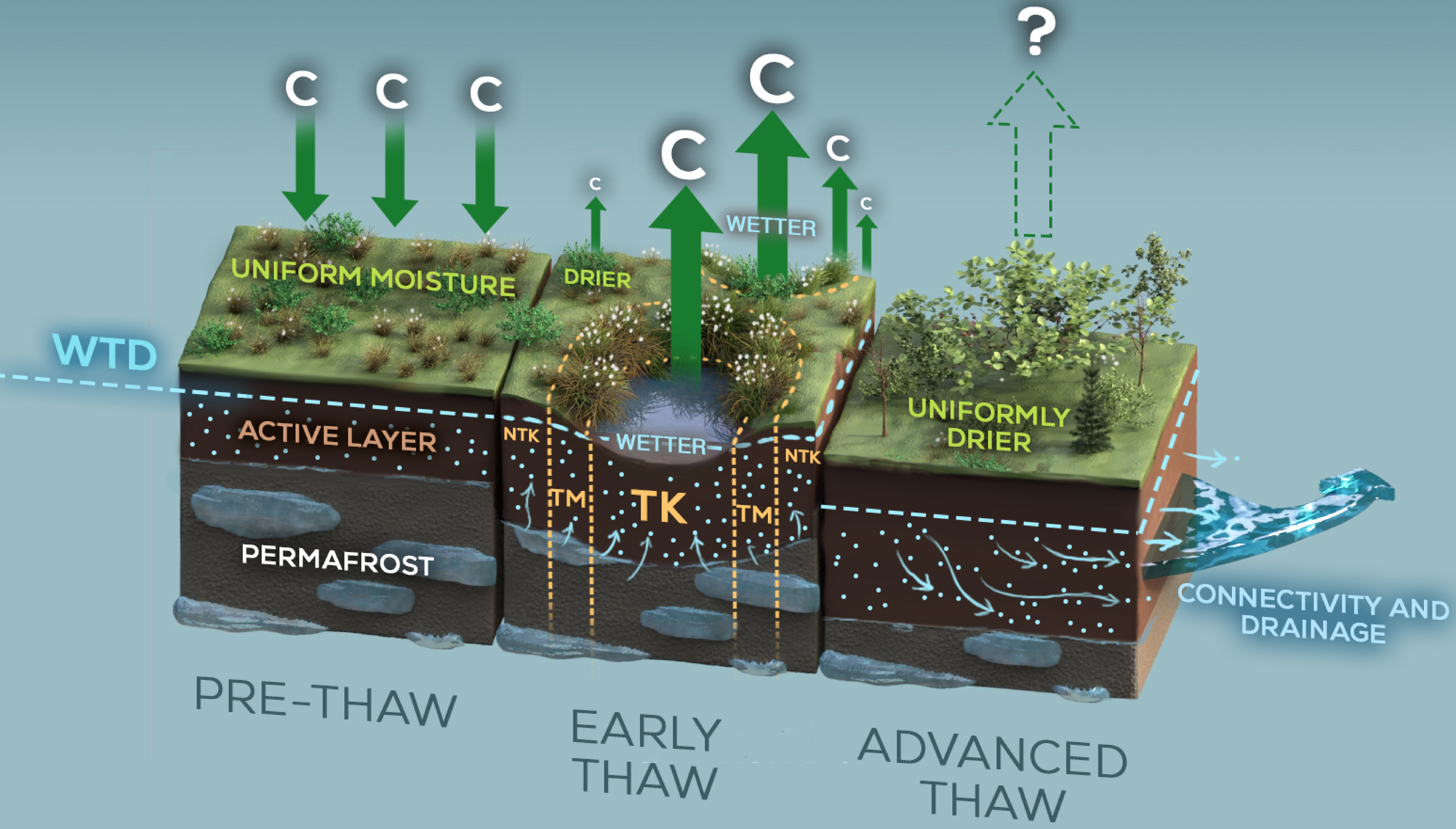
?
C
C
C
C
C
C
C
C
WETTER
UNIFORM MOISTURE
DRIER
WTD
ACTIVE LAYER
NTK
WETTER
NTK
TM
TK
TM
PERMAFROST
UNIFORMLY DRIER
CONNECTIVITY AND DRAINAGE
PRE-THAW
EARLY THAW
ADVANCED THAW

Supplemental Methods:

Rodenhizer et al. Abrupt Permafrost Thaw Drives Spatially Heterogeneous Soil Moisture and Carbon Dioxide Fluxes in Upland Tundra

Analysis of the Impact of Subsidence on Hydrology:

To determine the effect of subsidence on soil hydrologic conditions throughout the course of the experiment, we modeled the plot-level response of growing season mean and standard deviation of water table depth, surface moisture (0-5 cm), and soil moisture (0-15 cm) to subsidence using mixed effects models in the lme4 package (Bates et al., 2015). We included plot nested within treatment nested within snow fence nested within block as a random effect to account for the experimental design. To find the best fitting model, we considered models with 1) no fixed effects (null model), 2) subsidence, and 3) a quadratic subsidence effect. A quadratic term was tested to account for expected diminishing responses of hydrologic variables as subsidence proceeded and the inability of surface moisture and soil moisture to exceed 100%. Variable selection was performed using forward step-wise selection using AIC. Confidence intervals for fixed effects were bootstrapped with 1000 iterations using the MASS package and r^2 values were estimated using the MuMIn package (Bartoń, 2020). All variables were inspected for normality and an appropriate transformation was performed where necessary.

To investigate the intra-annual and spatial variability of the impact of subsidence on soil hydrologic conditions across plots for the entire experiment, we determined elevation, thaw depth, and water table depth along a transect spanning control and soil warming plots at each fence. Because each of these environmental variables were measured in slightly different locations across the experimental blocks, we used the kriged elevation (2.2.), and interpolated thaw depth and water table depth using universal kriging (incorporating the relationship between thaw depth or water table depth and subsidence) to get continuous surfaces from point measurements using the automap package (Hiemstra et al., 2009). Values from each layer were extracted along the transects using the raster package (Hijmans, 2021). Thaw depth and water table depth values were extracted both during a dry period and also following a large precipitation event; we selected dates that were about two weeks apart in 2018, because 2018 was the most recent year with both elevation data and a significant dry period. We used thaw depth measured on July 27, 2018 (dry) and Aug. 10, 2018 (wet) and water table depth measured on July 30, 2018 (dry) and Aug. 8, 2018 (wet). Because thaw depth and water table depth were not measured on exactly the same days, we chose dates that were as close in time as possible for comparison between thaw depth and water table depth (<= 3 days between measurements) while still falling within the window of dry and wet conditions. Elevation values were extracted only once, as the changes in elevation were negligible within the two week period.

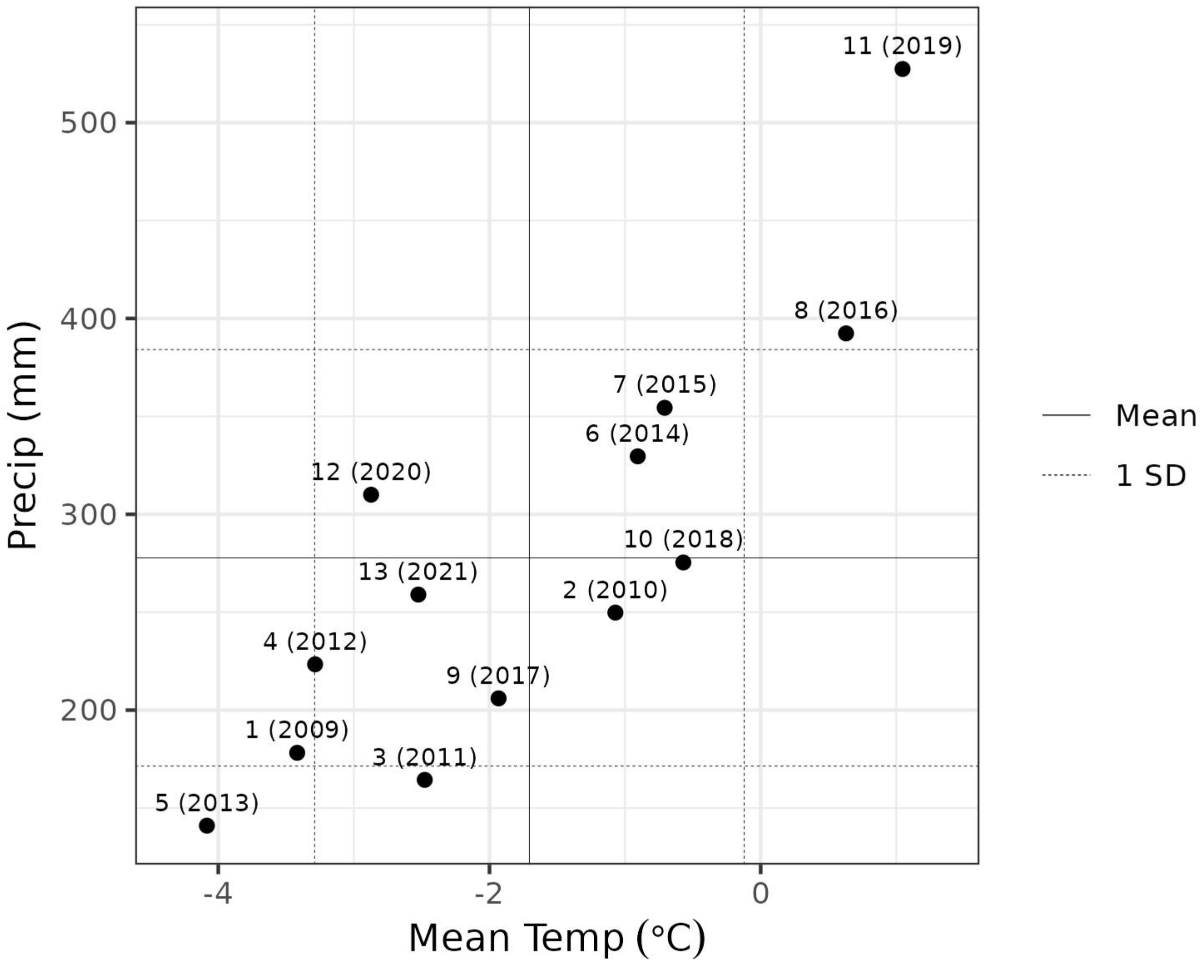

Figure S1. The spread of annual air temperature and precipitation conditions throughout the course of the warming experiment. Mean annual temperature was calculated from Oct. 1 (of the previous year) - Sept. 30 (of the year as labeled), while precipitation was calculated for the growing season, defined as May 1 - Sept. 30 (of the year as labeled). Mean and 1 standard deviation lines were calculated across all years.

Table S1. Growing season, non-growing season, and annual meteorological conditions at CiPEHR. Snow depth and snow free date are provided by treatment, as this varies among plots, while all other variables are provided at the site level only.

		Year												
		1	**2**	**3**	**4**	**5**	**6**	**7**	**8**	**9**	**10**	**11**	**12**	**13**
Measurement	**Season**	2009	2010	2011	2012	2013	2014	2015	2016	2017	2018	2019	2020	2021
Mean Air Temperature (°C)	Annual	-3.42	-1.07	-2.48	-3.29	-4.08	-0.91	-0.71	0.63	-1.93	-0.57	1.05	-2.87	-2.52
	Growing season	9.71	9.84	9.42	9.14	9.27	9.14	9.52	10.29	10.42	9.66	10.82	9.83	9.05
	Non-growing season	-12.92	-8.4	-11.07	-12.21	-13.72	-8.16	-8.09	-6.31	-10.85	-7.96	-6.01	-11.99	-10.88
Mean PAR (μmol m^{-2} s^{-1})	Annual	266.15	204.91	224.98	225.15	247.7	214.33	215.66	212.71	242.91	232.71	216.21	219.22	229.06
	Growing season	376.59	362.42	378.7	365.19	415.4	344.81	358.25	345.84	384.26	377.79	359.2	360.37	373.62
	Non-growing season	140.91	71.59	114.04	124.55	126.67	120.16	112.75	117.09	140.9	128.01	113.01	117.83	124.74
Rainfall (mm)	Annual	178.2	249.8	164.4	223.4	141	329.6	354.4	392.4	206	275.4	527.4	310	259
	Growing season	178.2	249.8	164.4	223.4	111.6	312.2	354.4	392.4	187.2	275.4	518.4	293.2	257.6
	Non-growing season	0	0	0	0	29.4	17.4	0	0	18.8	0	9	16.8	1.4
	Treatment													
Spring Snow Depth (m)	Air + Soil Warming	1.35 ± 0.12	0.49 ± 0.16	1.08 ± 0.16	1.29 ± 0.12	1.24 ± 0.13	0.79 ± 0.26	0.92 ± 0.2	1.13 ± 0.17	1.22 ± 0.11	1.55 ± 0.14	1.03 ± 0.22	1.32 ± 0.15	1.56 ± 0.13
	Air Warming	0.4 ± 0.11	0.18 ± 0.06	0.23 ± 0.05	0.55 ± 0.07	0.65 ± 0.12	0.22 ± 0.08	0 ± 0	0.3 ± 0.04	0.48 ± 0.06	0.83 ± 0.11	0.08 ± 0.12	0.59 ± 0.06	0.86 ± 0.1
	Control	0.4 ± 0.1	0.17 ± 0.06	0.23 ± 0.05	0.55 ± 0.08	0.65 ± 0.09	0.23 ± 0.07	0 ± 0	0.3 ± 0.08	0.49 ± 0.07	0.83 ± 0.13	0.09 ± 0.12	0.59 ± 0.07	0.86 ± 0.12
	Soil Warming	1.36 ± 0.08	0.7 ± 0.34	1.1 ± 0.23	1.29 ± 0.13	1.24 ± 0.08	0.94 ± 0.39	1.09 ± 0.38	1.22 ± 0.2	1.23 ± 0.13	1.58 ± 0.13	1.16 ± 0.3	1.32 ± 0.12	1.59 ± 0.12
Snow Free Date (DOY)	Air + Soil Warming	NA	118 ± 1	119 ± 0	125 ± 1	148 ± 1	109 ± 2	112 ± 1	111 ± 2	119 ± 2	133 ± 1	117 ± 3	121 ± 2	129 ± 1
	Air Warming	NA	117 ± 0	117 ± 1	126 ± 2	148 ± 1	110 ± 3	112 ± 0	108 ± 3	121 ± 2	131 ± 1	111 ± 0	123 ± 2	128 ± 1
	Control	NA	117 ± 0	117 ± 1	125 ± 1	148 ± 1	110 ± 2	112 ± 0	108 ± 3	121 ± 2	131 ± 1	111 ± 0	125 ± 3	128 ± 1
	Soil Warming	NA	117 ± 0	119 ± 0	125 ± 2	148 ± 1	109 ± 2	112 ± 1	111 ± 2	121 ± 3	133 ± 3	112 ± 2	121 ± 2	129 ± 1

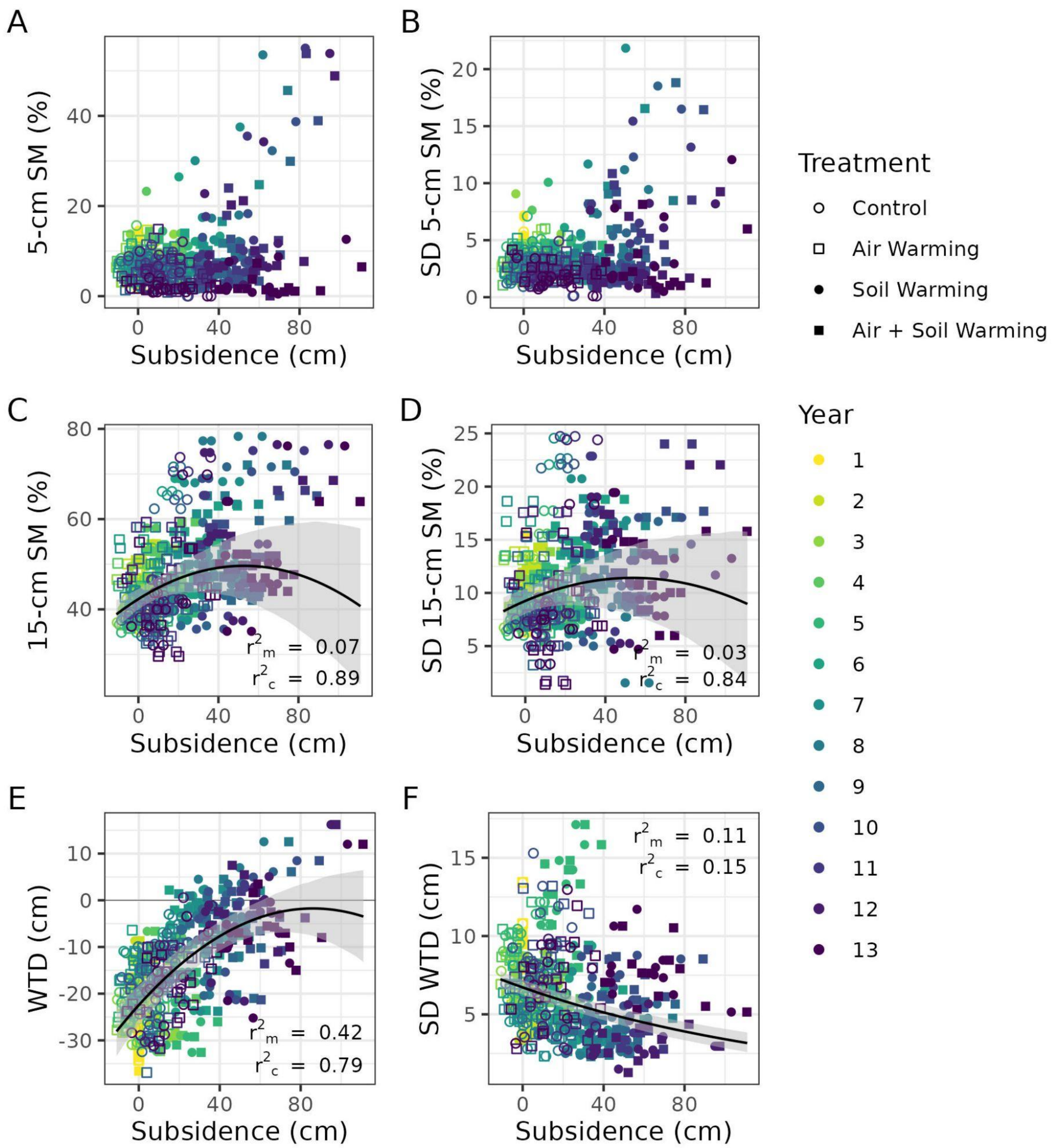

Figure S2. Scatterplots of subsidence by A) surface moisture, B) the standard deviation of surface moisture, C) soil moisture, D) the standard deviation of soil moisture, E) water table depth, and F) the standard deviation of water table depth. Points reflect plot-level mean annual values. Mixed effects models of the relationships are shown where statistically significant. The standard deviation of water table depth was log-transformed and quadratic terms were included in the relationships with soil moisture, the standard deviation of soil moisture, and water table depth. Low marginal r^2 combined with high conditional r^2 indicates the model fits very well on a plot by plot basis but that differences in the relationship between plots results in poor model fit when all plots are considered together.

Table S2. Model summaries of the mixed-effects linear models of water table depth, the standard deviation (SD) of water table depth, soil moisture, and the standard deviation of soil moisture by subsidence. Min and max values are the 95% confidence intervals for the coefficients and marginal and conditional r^2 values are indicated by r^2_m and r^2_c, respectively. Low marginal r^2 combined with high conditional r^2 indicates the model fits very well on a plot by plot basis but that differences in the relationship between plots results in poor model fit when all plots are considered together.

Response	**Final Variables**	**Coefficient**	**Min**	**Max**	**r^2_m**	**r^2_c**
Water Table Depth	Intercept	-22.5	-26.8	-18.1	0.416	0.793
	Subsidence	-0.00279	-0.00389	-0.00168		
	Subsidence^2	0.481	0.386	0.576		
SD Water Table Depth	Intercept	1.9	1.83	1.97	0.115	0.154
	Subsidence	-0.00679	-0.00847	-0.005		
Soil Moisture	Intercept	42.3	39.8	44.6	0.0707	0.889
	Subsidence	-0.00264	-0.00351	-0.0018		
	Subsidence^2	0.279	0.128	0.432		
SD Soil Moisture	Intercept	9.25	8.14	10.4	0.033	0.839
	Subsidence	-0.000749	-0.00116	-0.000352		
	Subsidence^2	0.0806	0.0205	0.139		

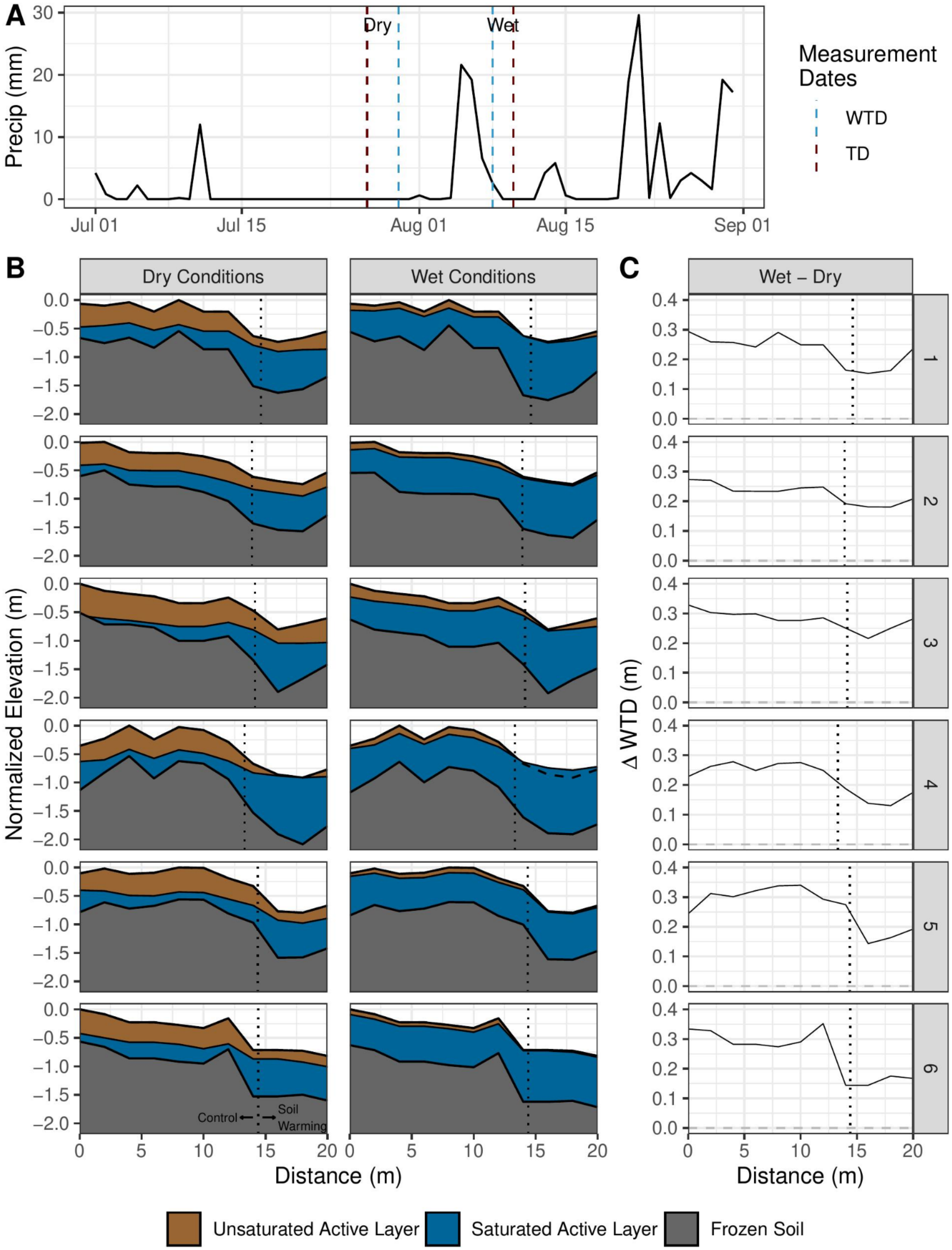
A
Precip (mm)
30
20
10
0
Jul 01
Jul 15
Aug 01
Aug 15
Sep 01
Dry
Wet
Measurement Dates
WTD
TD
B
Dry Conditions
Wet Conditions
Normalized Elevation (m)
0.0
−0.5
−1.0
−1.5
−2.0
Control
Soil Warming
Distance (m)
0
5
10
15
20
C
Wet – Dry
Δ WTD (m)
0.4
0.3
0.2
0.1
0.0
1
2
3
4
5
6
Unsaturated Active Layer
Saturated Active Layer
Frozen Soil

Figure S3. A) July and August precipitation in 2018, with water table depth (WTD) and thaw depth (TD) measurement dates marked for a period with dry conditions and a period with wet conditions. B) Elevation, thaw depth, and water table depth along control-soil warming transects at each of the 6 replicate snow fences during dry conditions and wet conditions. Gray fill indicates frozen soil at time of measurement (some of which is permafrost and some of which is frozen active layer), blue fill indicates fully saturated soils in the active layer, and brown indicates unsaturated soils in the active layer. The location of the snow fence is indicated with the dotted line with the control side to the left and the soil warming side to the right. C) The difference in water table depth before and after the precipitation event.

Figure S4. Photos from experimental set-up at block A in 2008, when thermokarst processes were not visible within the experimental footprint, and from block B in 2023, when thermokarst features dominated the experimental footprint. Areas of Non-TK, TK-margin and TK-center are indicated with arrows in the 2023 photo.

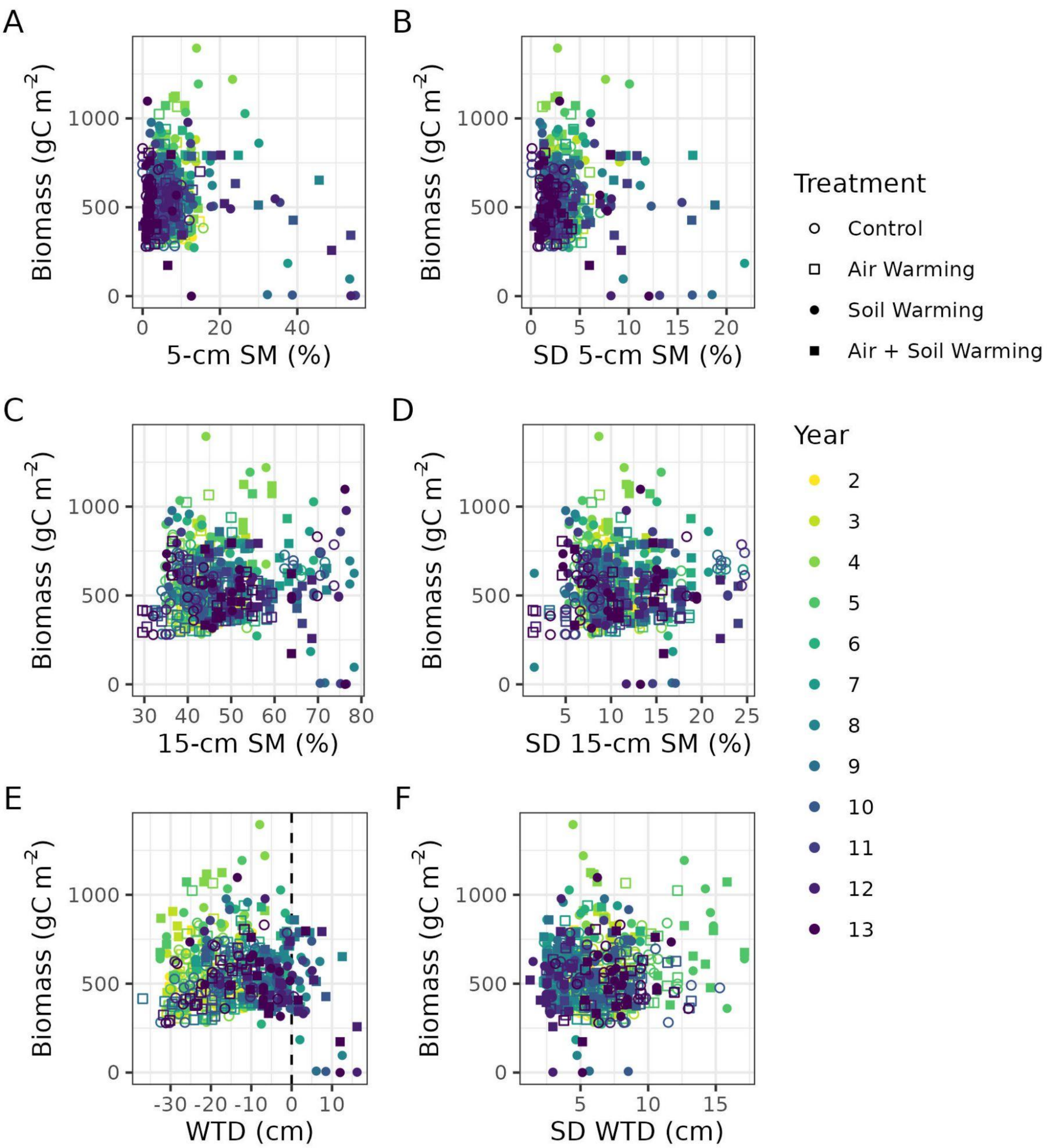

Figure S5. Scatterplots of AG Biomass by A) surface moisture, B) the standard deviation of surface moisture, C) soil moisture, D) the standard deviation of soil moisture, E) water table depth, and F) the standard deviation of water table depth. Points reflect annual average values for a single plot, with color indicating year and shape indicating treatment.

Table S3. Summary statistics from Figure 5. The mean value and spline prediction of NEE, R_{eco}, and GPP are shown for each thermokarst class at three stages: initial, peak, and final conditions. The year of each stage is also provided and, for peak values, may differ slightly between measured values and spline predictions.

		NEE				**R_{eco}**				**GPP**			
		Measured		**Spline**		**Measured**		**Spline**		**Measured**		**Spline**	
TK Class	**Stage**	**Year**	**Mean**	**Year**	**Prediction**	**Year**	**Mean**	**Year**	**Prediction**	**Year**	**Mean**	**Year**	**Prediction**
Non-TK	Initial	2	24 ± 26	2	41 ± 28	2	288 ± 28	2	280 ± 42	2	312 ± 29	2	313 ± 56
Non-TK	Peak	11	103 ± 19	10	86 ± 17	12	455 ± 82	13	428 ± 42	12	541 ± 79	13	502 ± 56
Non-TK	Final	13	58 ± 43	13	82 ± 28	13	415 ± 62	13	428 ± 42	13	477 ± 78	13	502 ± 56
TK Margin	Initial	2	49 ± 37	2	67 ± 30	2	288 ± 22	2	276 ± 31	2	337 ± 47	2	344 ± 45
TK Margin	Peak	9	135 ± 51	7	117 ± 19	7	393 ± 57	9	374 ± 20	9	524 ± 77	8	485 ± 28
TK Margin	Final	13	76 ± 30	13	90 ± 30	13	358 ± 46	13	358 ± 31	13	439 ± 63	13	441 ± 45
TK Center	Initial	2	42 ± 18	2	50 ± 29	2	315 ± 19	2	319 ± 32	2	357 ± 21	2	368 ± 48
TK Center	Peak	5	141 ± 34	5	124 ± 20	9	438 ± 55	8	417 ± 20	5	540 ± 57	6	524 ± 31
TK Center	Final	13	46 ± 27	13	55 ± 29	13	390 ± 50	13	388 ± 32	13	442 ± 64	13	440 ± 48

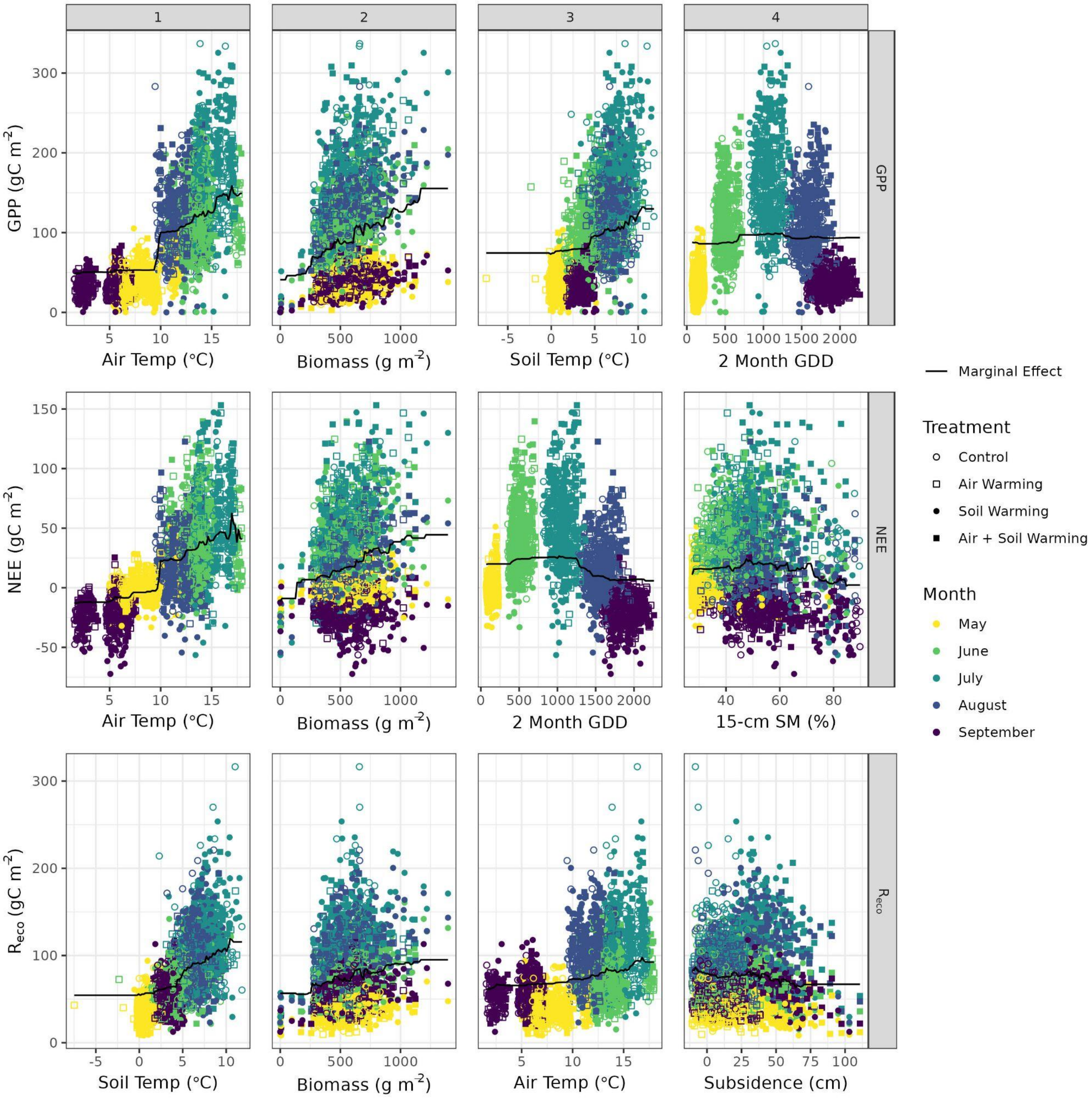

Figure S6. Partial dependence plots overlaid on measured data for the top four predictors of monthly GPP, NEE, and R_{eco} from the regression trees. Labels 1 through 4 indicate the order of predictor importance. Each point represents an individual plot over one month of measurements. Color indicates month and shape indicates treatment. Abbreviations are as follows: GDD = growing degree days, 15-cm SM = 0-15 cm soil moisture.

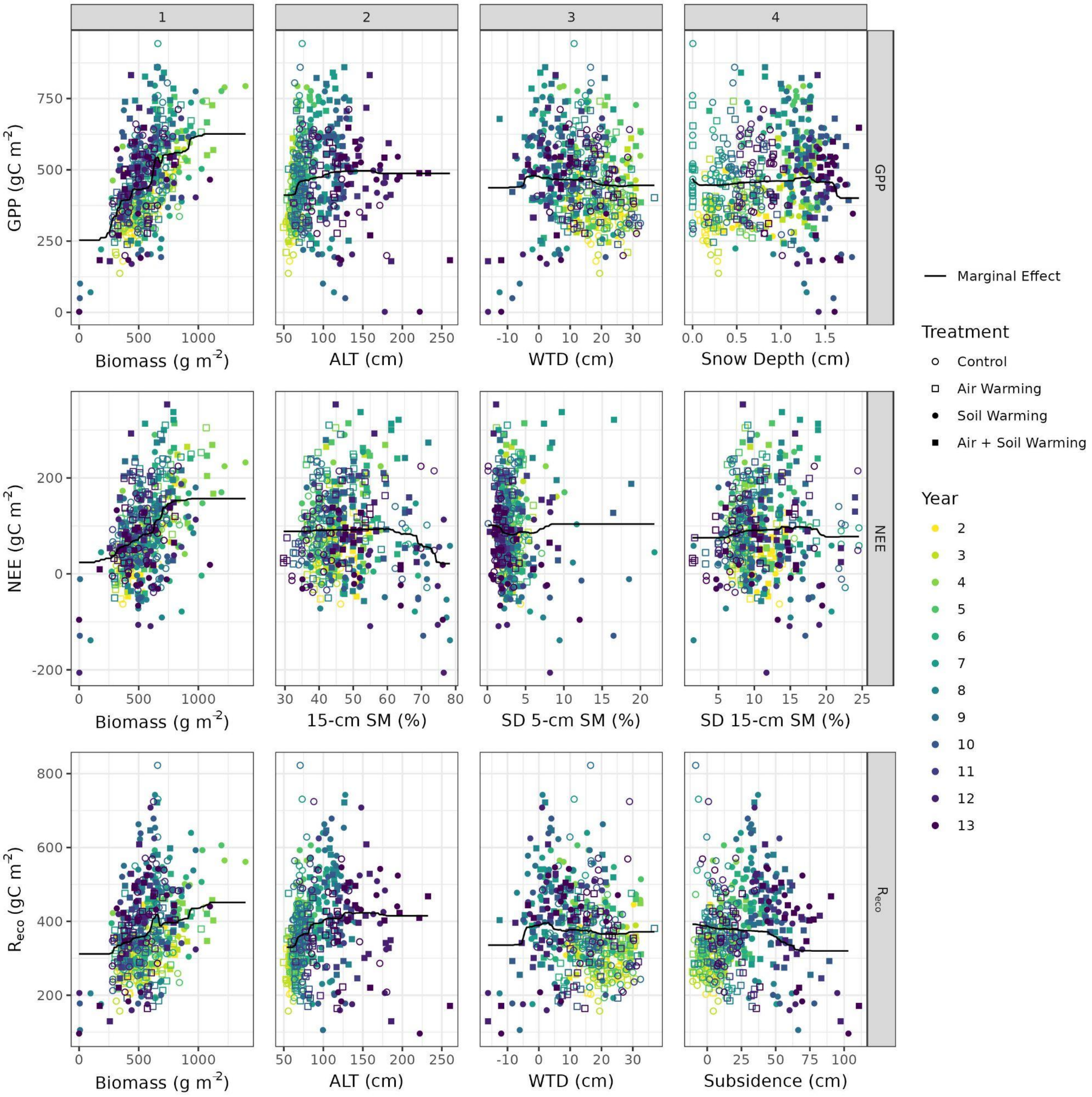

Figure S7. Partial dependence plots overlaid on measured data for the top four predictors of seasonal GPP, NEE, and R_{eco} from the regression trees. Each point represents an individual plot over one month of measurements. Color indicates month and shape indicates treatment. Abbreviations are as follows: SD = standard deviation, ALT = active layer thickness, WTD = water table depth, 15-cm SM = 0-15 cm soil moisture, 5-cm SM = 0-5 cm surface moisture.

Table S4. Growing season, non-growing season, and annual cumulative NEE, R_{eco}, and GPP throughout the course of the permafrost warming experiment. growing season values were calculated from gap-filled measurements. Winter NEE was estimated half-hourly using 5 cm soil temperature and the relationship between 5 cm soil temperature and winter NEE measured at an eddy covariance tower located approximately 1 km from the warming experiment. Each point represents the annual cumulative CO_2 flux for an individual plot. Color indicates plot-level AG Biomass. In 2019, only a subset of plots were measured for CO_2 fluxes, so annual sums were gap filled using monthly gradient boosted regression tree models of each CO_2 flux and plot-level environmental conditions.

Year	Treatment	NEE			Reco			GPP		
		Growing Season	Non-Growing Season	Annual	Growing Season	Non-Growing Season	Annual	Growing Season	Non-Growing Season	Annual
1 (2009)	Control	7 ± 21	-165 ± 23	-158 ± 31	197 ± 21	165 ± 23	363 ± 31	204 ± 21	0 ± 23	204 ± 31
	Air Warming	13 ± 34	-167 ± 11	-154 ± 36	234 ± 34	167 ± 11	401 ± 36	247 ± 34	0 ± 11	247 ± 36
	Soil Warming	-2 ± 24	-188 ± 12	-190 ± 27	212 ± 24	188 ± 12	400 ± 27	209 ± 24	0 ± 12	209 ± 27
	Air + Soil Warming	2 ± 37	-185 ± 13	-183 ± 39	239 ± 37	185 ± 13	424 ± 39	241 ± 37	0 ± 13	241 ± 39
2 (2010)	Control	23 ± 38	-148 ± 8	-125 ± 39	267 ± 38	148 ± 8	415 ± 39	290 ± 38	0 ± 8	290 ± 39
	Air Warming	45 ± 54	-145 ± 9	-100 ± 55	303 ± 54	145 ± 9	448 ± 55	348 ± 54	0 ± 9	348 ± 55
	Soil Warming	48 ± 54	-167 ± 10	-119 ± 55	330 ± 54	167 ± 10	497 ± 55	378 ± 54	0 ± 10	378 ± 55
	Air + Soil Warming	47 ± 61	-162 ± 13	-115 ± 62	311 ± 61	162 ± 13	473 ± 62	357 ± 61	0 ± 13	357 ± 62
3 (2011)	Control	49 ± 36	-151 ± 9	-102 ± 38	235 ± 36	151 ± 9	386 ± 38	283 ± 36	0 ± 9	283 ± 38
	Air Warming	76 ± 63	-149 ± 9	-74 ± 64	280 ± 63	149 ± 9	429 ± 64	356 ± 63	0 ± 9	356 ± 64
	Soil Warming	102 ± 61	-184 ± 12	-82 ± 62	342 ± 61	184 ± 12	526 ± 62	444 ± 61	0 ± 12	444 ± 62
	Air + Soil Warming	93 ± 97	-188 ± 12	-95 ± 98	302 ± 97	188 ± 12	490 ± 98	395 ± 97	0 ± 12	395 ± 98
4 (2012)	Control	76 ± 40	-166 ± 17	-90 ± 44	301 ± 40	166 ± 17	467 ± 44	377 ± 40	0 ± 17	377 ± 44
	Air Warming	98 ± 84	-164 ± 15	-66 ± 85	326 ± 84	164 ± 15	490 ± 85	424 ± 84	0 ± 15	424 ± 85
	Soil Warming	126 ± 75	-197 ± 9	-71 ± 76	446 ± 75	197 ± 9	644 ± 76	573 ± 75	0 ± 9	573 ± 76
	Air + Soil Warming	113 ± 88	-196 ± 13	-83 ± 89	384 ± 88	196 ± 13	580 ± 89	497 ± 88	0 ± 13	497 ± 89
5 (2013)	Control	98 ± 39	-187 ± 15	-89 ± 41	299 ± 39	187 ± 15	486 ± 41	397 ± 39	0 ± 15	397 ± 41
	Air Warming	122 ± 90	-187 ± 12	-65 ± 91	311 ± 90	187 ± 12	498 ± 91	433 ± 90	0 ± 12	433 ± 91
	Soil Warming	147 ± 81	-201 ± 9	-54 ± 82	458 ± 81	201 ± 9	659 ± 82	605 ± 81	0 ± 9	605 ± 82
	Air + Soil Warming	129 ± 104	-197 ± 15	-68 ± 106	364 ± 104	197 ± 15	561 ± 106	493 ± 104	0 ± 15	493 ± 106
6 (2014)	Control	105 ± 44	-196 ± 8	-91 ± 45	339 ± 44	196 ± 8	535 ± 45	445 ± 44	0 ± 8	445 ± 45
	Air Warming	119 ± 86	-200 ± 11	-82 ± 86	313 ± 86	200 ± 11	513 ± 86	432 ± 86	0 ± 11	432 ± 86
	Soil Warming	83 ± 65	-219 ± 7	-136 ± 66	430 ± 65	219 ± 7	650 ± 66	514 ± 65	0 ± 7	514 ± 66

	Air + Soil Warming	109 ± 100	-217 ± 12	-108 ± 101	411 ± 100	217 ± 12	628 ± 101	521 ± 100	0 ± 12	521 ± 101
7 (2015)	Control	104 ± 70	-186 ± 8	-82 ± 71	408 ± 70	186 ± 8	594 ± 71	512 ± 70	0 ± 8	512 ± 71
	Air Warming	129 ± 102	-190 ± 8	-62 ± 102	357 ± 102	190 ± 8	548 ± 102	486 ± 102	0 ± 8	486 ± 102
	Soil Warming	81 ± 85	-220 ± 6	-139 ± 86	405 ± 85	220 ± 6	625 ± 86	486 ± 85	0 ± 6	486 ± 86
	Air + Soil Warming	163 ± 139	-220 ± 8	-57 ± 139	424 ± 139	220 ± 8	644 ± 139	588 ± 139	0 ± 8	588 ± 139
8 (2016)	Control	84 ± 72	-196 ± 6	-113 ± 72	415 ± 72	196 ± 6	611 ± 72	502 ± 72	0 ± 6	502 ± 72
	Air Warming	94 ± 81	-196 ± 11	-102 ± 81	322 ± 81	196 ± 11	518 ± 81	419 ± 81	0 ± 11	419 ± 81
	Soil Warming	-4 ± 73	-228 ± 6	-232 ± 73	455 ± 73	228 ± 6	683 ± 73	455 ± 73	0 ± 6	455 ± 73
	Air + Soil Warming	99 ± 108	-227 ± 6	-128 ± 108	463 ± 108	227 ± 6	690 ± 108	565 ± 108	0 ± 6	565 ± 108
9 (2017)	Control	96 ± 64	-163 ± 13	-66 ± 65	426 ± 64	163 ± 13	588 ± 65	524 ± 64	0 ± 13	524 ± 65
	Air Warming	126 ± 91	-169 ± 11	-43 ± 92	343 ± 91	169 ± 11	512 ± 92	471 ± 91	0 ± 11	471 ± 92
	Soil Warming	48 ± 81	-189 ± 11	-141 ± 82	465 ± 81	189 ± 11	654 ± 82	516 ± 81	0 ± 11	516 ± 82
	Air + Soil Warming	154 ± 72	-190 ± 7	-36 ± 72	439 ± 72	190 ± 7	629 ± 72	596 ± 72	0 ± 7	596 ± 72
10 (2018)	Control	75 ± 58	-212 ± 7	-137 ± 59	362 ± 58	212 ± 7	574 ± 59	438 ± 58	0 ± 7	438 ± 59
	Air Warming	125 ± 64	-214 ± 8	-89 ± 65	308 ± 64	214 ± 8	522 ± 65	434 ± 64	0 ± 8	434 ± 65
	Soil Warming	19 ± 81	-229 ± 5	-210 ± 81	412 ± 81	229 ± 5	641 ± 81	433 ± 81	0 ± 5	433 ± 81
	Air + Soil Warming	101 ± 69	-229 ± 4	-128 ± 69	399 ± 69	229 ± 4	628 ± 69	502 ± 69	0 ± 4	502 ± 69
11 (2019)	Control	111 ± 61	-189 ± 6	-78 ± 61	381 ± 61	189 ± 6	569 ± 61	459 ± 61	0 ± 6	459 ± 61
	Air Warming	97 ± 27	-188 ± 10	-92 ± 28	381 ± 27	188 ± 10	569 ± 28	458 ± 27	0 ± 10	458 ± 28
	Soil Warming	76 ± 61	-211 ± 6	-135 ± 61	438 ± 61	211 ± 6	649 ± 61	481 ± 61	0 ± 6	481 ± 61
	Air + Soil Warming	102 ± 57	-211 ± 7	-109 ± 58	405 ± 57	211 ± 7	617 ± 58	512 ± 57	0 ± 7	512 ± 58
12 (2020)	Control	105 ± 79	-202 ± 12	-98 ± 79	442 ± 79	202 ± 12	644 ± 79	521 ± 79	0 ± 12	521 ± 79
	Air Warming	147 ± 70	-205 ± 15	-58 ± 71	323 ± 70	205 ± 15	527 ± 71	446 ± 70	0 ± 15	446 ± 71
	Soil Warming	2 ± 102	-227 ± 6	-224 ± 102	403 ± 102	227 ± 6	630 ± 102	399 ± 102	0 ± 6	399 ± 102
	Air + Soil Warming	125 ± 100	-227 ± 4	-101 ± 100	381 ± 100	227 ± 4	608 ± 100	492 ± 100	0 ± 4	492 ± 100
13 (2021)	Control	59 ± 74	-211 ± 8	-152 ± 75	389 ± 74	211 ± 8	601 ± 75	452 ± 74	0 ± 8	452 ± 75
	Air Warming	96 ± 51	-213 ± 12	-117 ± 52	363 ± 51	213 ± 12	576 ± 52	463 ± 51	0 ± 12	463 ± 52
	Soil Warming	0 ± 62	-228 ± 8	-227 ± 63	394 ± 62	228 ± 8	622 ± 63	400 ± 62	0 ± 8	400 ± 63
	Air + Soil Warming	71 ± 39	-224 ± 6	-154 ± 40	398 ± 39	224 ± 6	623 ± 40	475 ± 39	0 ± 6	475 ± 40

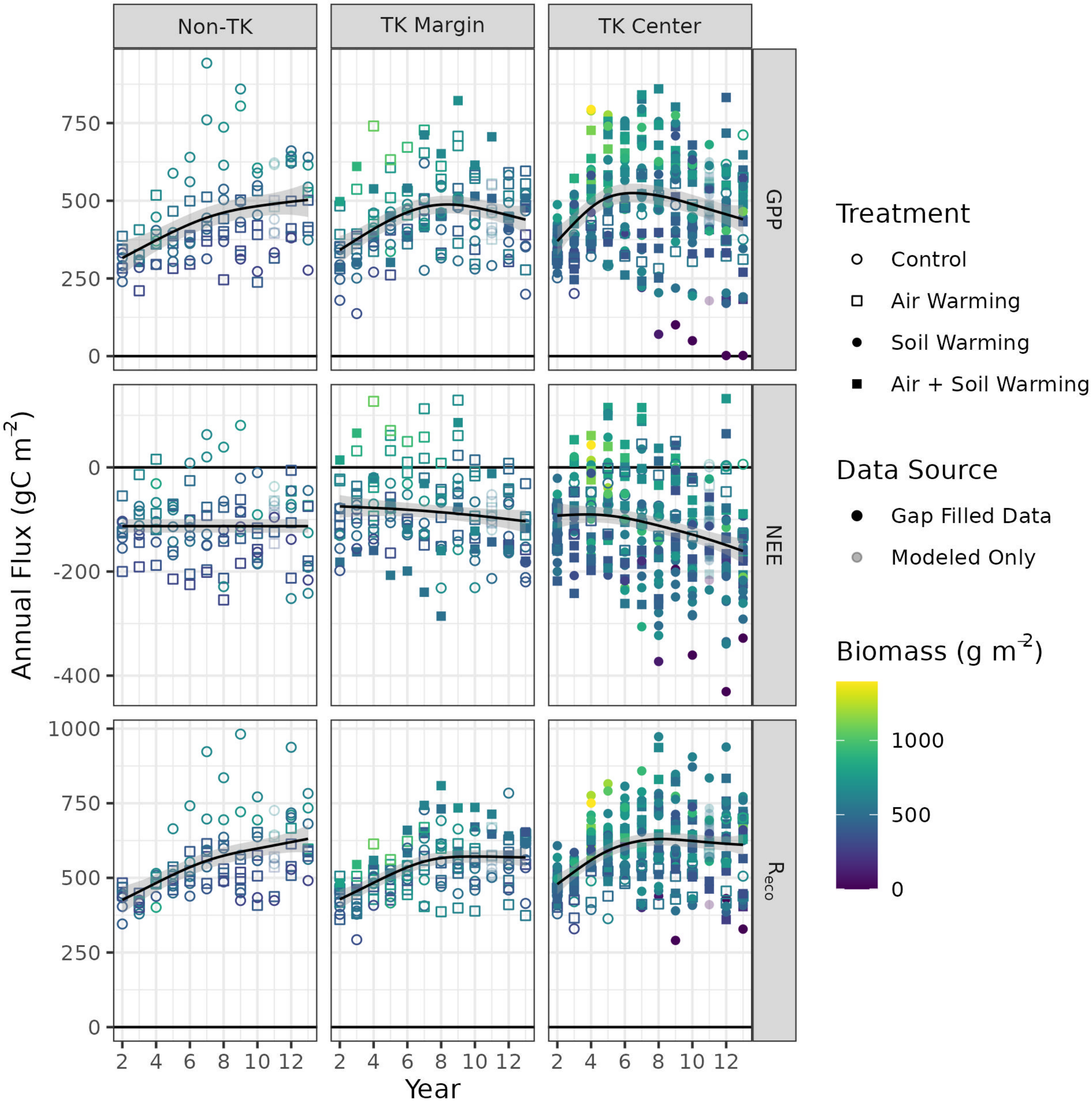

Figure S8. The trajectory of annual CO_2 fluxes throughout the course of the warming experiment in each of the thermokarst classes with splines to highlight trends through time. Each plot was assigned to the same thermokarst class in all years based on the thermokarst class in 2021. Each point represents the annual cumulative CO_2 flux for an individual plot. Color indicates plot-level AG Biomass and shape indicates experimental treatment. Solid points indicate growing season sums of gap-filled measurements, and transparent points in 2019 indicate growing season sums which were modeled using the monthly regression trees of each CO_2 flux and plot-level environmental conditions.

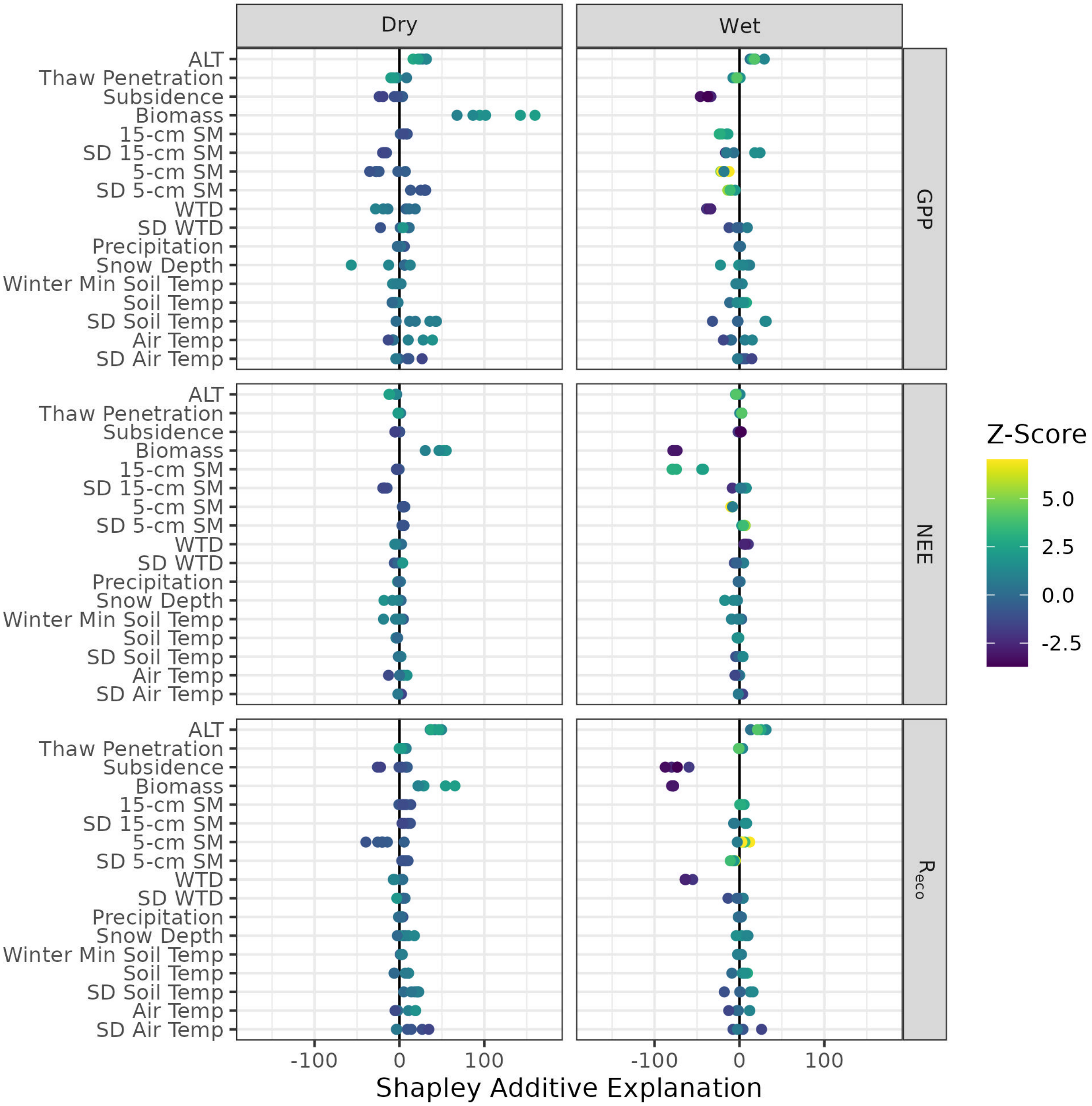

Figure S9. Shapley additive explanation values for cumulative growing season fluxes in a deeply thawed and dry (Dry) plot and a deeply thawed and wet (Wet) plot for the years 2016-2021. Shapley values indicate the importance of each variable in the GBM prediction for a single response value. A positive Shapley value indicates a higher flux resulting from the observed value of the explanatory variable. Note that a positive Shapley value only indicates a positive relationship between the explanatory variable and the flux in the case when the explanatory variable is higher than average, otherwise it indicates a negative relationship. Z-scores indicate the value of the explanatory variable for that observation. Abbreviations are as follows: SD = standard deviation, ALT = active layer thickness, WTD = water table depth, 15-cm SM = 0-15 cm soil moisture, 5-cm SM = 0-5 cm surface moisture.